Heteronanotrimers by selective photodeposition of gold nanodots on Janus-Type Cu2-x/CuInS2 heteronanocrystals

Fenghuan Zhao, Chenghui Xia, Junjie Hao, Celso de Mello Donegá, Marie-hélène Delville, Jean-Pierre Delville

NANO · MICRO small
www.small-journal.com

Heteronanotrimers by Selective Photodeposition of Gold Nanodots on Janus-Type $Cu_{2-x}S/CuInS_2$ Heteronanocrystals

Fenghuan Zhao, Chenghui Xia, Junjie Hao, Celso de Mello Donegá, Marie-Hélène Delville, and Jean-Pierre Delville**

This study focuses on the development of environmentally friendly Au-$Cu_{2-x}S/CuInS_2$ heteronanotrimers. The chosen strategy relies on the laser photodeposition of a single gold nanodot (ND) onto Janus $Cu_{2-x}S/CuInS_2$ heteronanocrystals (HNCs). This method offers precise control over the number, location, and size (5 to 8 nm) of the Au NDs by adjusting laser power for the career production, concentration of hole scavenger for charge equilibration in redox reactions, and gold precursor concentration, and exposure time for the final ND size. The photoreduction of gold ions onto HNCs starts systematically at the $Cu_{2-x}S$ tip. The Au deposition then depends on the $CuInS_2$ segment length. For short HNCs, stable Au-$Cu_{2-x}S/CuInS_2$ heteronanotrimers form, while long HNCs undergo a secondary photo-induced step: the initial Au ND is progressively oxidized, with concomitant deposition of a second gold ND on the $CuInS_2$ side, to yield Au_2S-$Cu_{2-x}S/CuInS_2$-Au heteronanotrimers. Results are rationalized by quantitative comparison with a model that describes the growth kinetics of NDs and Au-$Cu_{2-x}S$ transformation and emphasizes the importance of charge separation in predicting selective deposition in heteronanotrimer production. The key parameter controlling Au-$Cu_{2-x}S/CuInS_2$ HNCs is the photoinduced electric field gradient generated by charge separation, which is tailored by controlling the $CuInS_2$ segment size.

1. Introduction

Colloidal metal-semiconductor hybrid nanocrystals (NCs) present many advantages. They are highly effective in boosting light harvesting and conversion in surface-enhanced Raman spectroscopy.[1] They have been used in biomedical applications in conjugation with photodynamic therapy[2] or in hydrogels for wound healing.[3] They are also used in photocatalytic applications, such as alternative clean solar-to-fuel conversion;[4] examples include hydrogen generation via photocatalytic water splitting and photocatalytic CO_2 reduction.[5] They indeed attracted particular interest in recent years because they usually exhibit superior photocatalytic performances compared to either component alone thanks to synergistic interactions, wherein the semiconductors provide tunable optical bandgaps and high photogenerated carrier density while the metal domains drastically enhance the reducing and catalytic properties.[6–8] This is generally due to the formation of a Schottky junction, which promotes charge separation and charge transfer when metal nanodots (NDs) and semiconductors are in close contact.[6,7,9]

To date, most metal-semiconductor hybrid NCs use metal oxides and Cd-based chalcogenides. Although metal oxides such as TiO_2, WO_3, and ZnO exhibit excellent stability and photocatalytic activity, their wide band gaps confine their effectiveness to the ultra-violet (UV) spectral range, limiting the optimal exploitation of sunlight irradiation.[7,9,10] Conversely, Cd-based

F. Zhao, J. Hao, M.-H. Delville
CNRS
Univ. Bordeaux
Bordeaux INP
ICMCB
UMR 5026, 87 avenue du Dr. A. Schweitzer, Pessac F-33608, France
E-mail: marie-helene.delville@icmcb.cnrs.fr

The ORCID identification number(s) for the author(s) of this article can be found under https://doi.org/10.1002/smll.202407045

DOI: 10.1002/smll.202407045

F. Zhao, J. Hao, J.-P. Delville
Univ. Bordeaux
CNRS
LOMA
UMR 5798, 351 Cours de la Liberation, Talence 33405, France
E-mail: jean-pierre.delville@u-bordeaux.fr

C. Xia, C. de M. Donegá
Condensed Matter and Interfaces
Debye Institute for Nanomaterials Science
Utrecht University
Utrecht 3508 TA, The Netherlands

C. Xia
School of Materials Science and Engineering
Ocean University of China
238 Songling Road, Qingdao 266100, P. R. China

J. Hao
Key Laboratory of Energy Conversion and Storage Technologies (Southern University of Science and Technology)
Ministry of Education
Shenzhen 518055, China

chalcogenides exhibit suitable band gaps in the visible region and demonstrate high photocatalytic efficiency.[8] However, their practical applications are severely restricted by intrinsic toxicity and poor photostability attributed to hole accumulation during photochemical reactions.[11,12]

Thus, NCs based on Cu-chalcogenide not only are an attractive alternative substrate with applications as lubricants/additives,[13] electrode materials,[14 15] co-catalysts,[16] but also constitute a platform to use with metal NDs for the construction of highly efficient functionalities since they exhibit lower toxicity, excellent photocatalytic activities, and compositionally tunable band gaps, that match well with the solar spectral range.[17–23] The most commonly reported metal-Cu chalcogenide hybrid NCs involve binary Cu-chalcogenides, such as Au–Cu_2S heteronanodimers,[18] Pt–$Cu_{2-x}S$ hybrid nanoplatelets,[19,20] Pt–$Cu_{2-x}Se$ and Au–$Cu_{2-x}Se$ heteronanodimers,[21] dual plasmonic Au@$Cu_{2-x}E$ (E = S, Se) core@shell superparticles,[22,23] and Au-$Cu_{2-x}Te$ disk-on-dot heterostructures.[24] Besides the advanced development of synthesis methods and the rich libraries of Cu-chalcogenide NCs, metal NDs have also been successfully extended to more complex heterostructures, e.g., Au deposited on ternary $CuInS_2$,[25–27] $CuGaS_2$,[28] $CuFeSe_2$[29] NCs, and quaternary Cu_2ZnSnS_4 nanostructures.[30–33] Although the presence of metal NDs on Cu-chalcogenide NCs improves their photocatalytic performance, their efficiency still lags far behind that of prototypical metal-decorated Cd-based semiconductors. For instance, Amirav's group reported that Pt-tipped CdSe@CdS nanorods (NRs) exhibited an impressive efficiency of 100% in producing hydrogen from photons under visible light illumination.[34]

One of the key factors influencing charge separation is the control of the flowing photogenerated electrons and holes. Compared to single-component copper chalcogenide semiconductors, axially segmented heteronanocrystals (HNCs), presenting a design with a type-II band alignment, are much more attractive because they have a configuration, which already leads to the efficient spatial separation of the electron-hole pairs under light irradiation. Achieving highly selective deposition of metal nanodots (NDs) on such a segmented nanostructure could enhance control over the directionality of charge carrier flow. However, most of the publications on metal ND deposition, to date, have been limited to the use of single-component Cu-chalcogenide NCs. To the best of our knowledge, single ND deposition on segmented multi-component Cu-chalcogenide HNCs remains to be demonstrated and confidently established. This work aims to address this gap.

We think that such a report has not been made before partly because Cu-chalcogenide HNCs are challenging to synthesize. This difficulty arises from two main factors: the fast diffusion rate of Cu^+ into the crystal lattice[35] and the difficulty in balancing the reactivity of cationic to anionic precursors.[36] Indeed, the cation exchange reaction used is a powerful tool for synthesizing various heteronanocrystals including $Cu_{2-x}S$-$CuInS_2$ heterojunctions.[37,38] However, it should be noted that this cation exchange reaction is a double-edged sword. Generally, the cation exchange reaction is topotactic by nature, and the produced nanocrystals exhibit well-preserved size and shape. If we consider the In^{3+} cation exchange for Cu^+ in $Cu_{2-x}S$ nanorod, the reaction site is hard to control, and the exchange can occur on the tips or sides of the nanorod. This uncertainty leads to the formation of HNCs lacking uniformity. For example, the In^{3+} for Cu^+ cation exchange in $Cu_{2-x}S$ nanorods reported by Zhai et al.[38] shows that the produced HNCs exhibit distinct heterostructure morphologies, such as Janus-type or multi-segmented HNCs. Moreover, the extent of the cation exchange reaction is also hard to control, and the final component may exhibit quite different volume percentages in the final product HNCs. This issue also exacerbates the uniformity of the heteronanorods. Last but not least, as the cation exchange reaction occurs in the template nanocrystals, the synthesis of Janus-type $Cu_{2-x}S/CuInS_2$ with various aspect ratios is highly restricted. To solve this problem, we propose to use a seeded-mediated growth method of $Cu_{2-x}S/CuInS_2$ HNCs. This method provides a versatile way to produce HNCs with excellent uniformity and flexibility.[39] On the one hand, compared to single-component Cu-chalcogenide NCs, $Cu_{2-x}S/CuInS_2$ HNCs have a sharp hetero-interface and can form a typical type-II heterojunction, which provides an ideal opportunity to study the selective deposition of single metal NDs. On the other hand, the nucleation and growth of this single Au ND on Janus-type $Cu_{2-x}S/CuInS_2$ HNCs are performed by laser photodeposition.[40] Indeed, beyond favoring metallic ND deposition[41] and offering a simple way to vary light intensity,[42] the coherence and directivity of continuous laser waves allow precise matching between beam and sample sizes. Their photon irradiance ability, up to several orders of magnitude higher than any common wide light source, can tremendously increase the production of electron-hole pairs at the same optical wavelength. This increased production makes the availability of electrons and holes for surface reactions and deposition almost insensitive to the unavoidable structural defects of HNCs. Finally, when a first deposit is nucleated at these high intensities, it automatically triggers high electric field gradients within the HNCs that strongly favor the deposit growth over secondary nucleation, which enhances, in return, electron-hole pair separation. Laser-deposition of Au NDs onto $Cu_{2-x}S/CuInS_2$ HNCs should, thus, be controllable spatially (e.g., number and location) and kinetically (e.g., growth rate and final size) by tuning the laser power, exposure time, concentration of gold precursor, and hole scavenger; such experimental control should allow quantitative comparisons with dedicated modeling. *Ex-situ* monitoring by transmission electron microscopy (TEM) demonstrates that laser deposition of single Au NDs on HNCs is indeed effective and exhibits excellent selectivity, consistently starting on the $Cu_{2-x}S$ part. A possible secondary nucleation process onto the $CuInS_2$ segment, concomitant with the oxidation of the Au^0 ND and the formation of Au_2S areas on the $Cu_{2-x}S$ segment, can also take place. We shall show that (i) this process depends on the overall length of the $Cu_{2-x}S/CuInS_2$ HNCs and that (ii) therefore, laser deposition offers an efficient route to synthesize Au-$Cu_{2-x}S/CuInS_2$ heteronanotrimers with both versatility and predictability.

2. Synthesis and Characterization of $Cu_{2-x}S/CuInS_2$ HNCs

$Cu_{2-x}S/CuInS_2$ HNCs with different lengths were synthesized by fast injection of a solution of preformed $Cu_{2-x}S$ seed nanodisks (diameter $D_0 = 19.3 \pm 1.8$ nm and height $h_0 = 8.7 \pm 0.6$ nm, $x = 0.4 \pm 0.05$) dispersed in dodecanethiol into a hot indium oleate

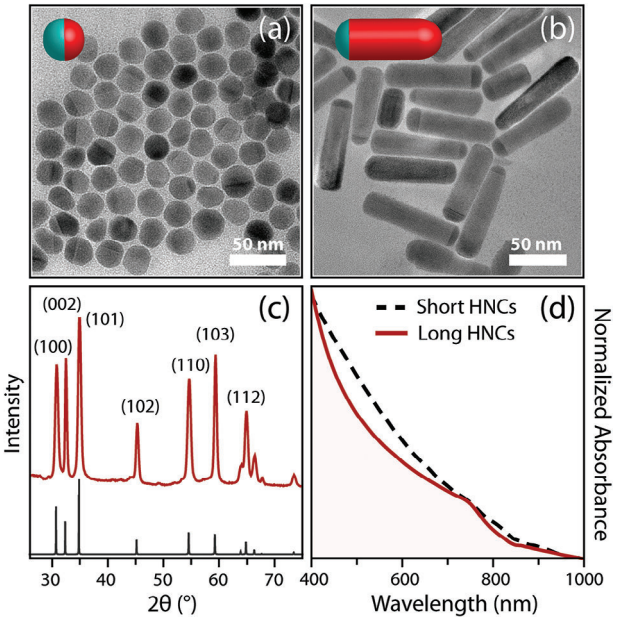

Figure 1. a,b) TEM images of short a) and long b) Janus-type $Cu_{2-x}S/CuInS_2$ HNCs. Insets are cartoon representations of the HNCs with the cyan part as $Cu_{2-x}S$ and the red one as $CuInS_2$. c) XRD pattern of the long Janus-type $Cu_{2-x}S/CuInS_2$ HNCs (red line). The XRD pattern of hexagonal wurtzite $CuInS_2$ (grey line, JCPDS Card n° 01-077-9459) is shown for reference. d) Normalized absorption spectra of short (black dashed line) and long (red solid line) Janus-type $Cu_{2-x}S/CuInS_2$ HNCs.

solution at 240 °C following a previously reported procedure (See: Method section for details).[39] TEM images (**Figure 1**a,b) show that short HNCs (D_0 = 19.3 ± 1.8 nm, $Cu_{2-x}S$ height h_0 = 8.5 ± 2.7 nm, overall length l_0 = 27.3 ± 12.6 nm) and long ones (diameter D_0 = 16.1 ± 2.6 nm, $Cu_{2-x}S$ height h_0 = 5.0 ± 1.4 nm, overall length l_0 = 74.0 ± 12.6 nm) exhibit the interparticle contrast due to the distinct components, namely, binary $Cu_{2-x}S$ (darker part) and ternary $CuInS_2$ (brighter part).[39] The X-ray diffraction pattern of the long HNCs (Figure 1c) shows that the diffraction peaks are dominated by the hexagonal wurtzite segment of $CuInS_2$ with no obvious contribution from the monoclinic tips of low chalcocite $Cu_{2-x}S$. This observation is likely due to the small volume of the $Cu_{2-x}S$ tip compared to that of the elongated $CuInS_2$ segment, and the similar hexagonal closed-packed S^{2-} sublattice in the low-chalcocite $Cu_{2-x}S$ and wurtzite $CuInS_2$.[39] The absorption spectrum of the long $Cu_{2-x}S/CuInS_2$ HNCs is slightly different from that of the short ones because of the larger volume of the elongated $CuInS_2$, which typically has a featureless absorption shoulder in the near-infrared region.[43] Both types of HNCs exhibit a broad absorption over a wide spectral range that spans the entire visible region (Figure 1d).

2.1. Laser-Induced Photodeposition of Au on $Cu_{2-x}S$ NCs and Short $Cu_{2-x}S/CuInS_2$ HNCs

Photodeposition experiments were performed in a 1 cm pathlength sealed quartz cuvette containing toluene with a mixture of oleic acid/dodecanethiol capped $Cu_{2-x}S$ NCs (seed nanocrystals, NCs) and $Cu_{2-x}S/CuInS_2$ (short HNCs) with a ratio $\frac{2}{3}$[HNC] + $\frac{1}{3}$ [NC] = 1.068×10^{-8} M. Dodecylamine-modified $KAuCl_4$ precursor[44] was then added in different ratios. We selected methanol (MeOH) as a hole scavenger because of its small size, good miscibility in non-polar toluene,[45] and high hole-trapping efficiency as demonstrated by the photodeposition of noble metals on Cd chalcogenide NCs[46] and TiO_2 nanoparticles.[40] Instead of conventional lamps/LEDs, we used a continuous laser working at 473 nm (MLL-N-473-300 mW, from CNI Company) as the irradiation source to efficiently and simultaneously excite $Cu_{2-x}S$ NCs and $Cu_{2-x}S/CuInS_2$ HNCs (Figure 1d). The beam power at the exit of the laser head could span the range P_L = 0 − 389 mW by increasing the driving current with a maximum availability of 5.0 A. After exiting the laser head, the beam size $2\omega_0$ is extended to ≈1 cm in diameter using a homemade telescope and then directed to the quartz cuvette filled with 1 mL of the solution to be fully irradiated. The setup transmission from the laser head to the cuvette is P_i/P_L = 81%, where P_i represents the power incident to the cuvette. The cuvette transmission, when filled with the reaction mixture, goes down to 47.9%; the power range in the middle of the cuvette thus varies in the range $P_{1/2}$ = 0 − 218 mW, hereafter called P, for the sake of simplicity. The solution is stirred continuously, at 300 rpm, under illumination at room temperature to ensure homogeneous dispersion during the reaction process. Readers can find an illustration and detailed description of the setup in ref. [46].

By giving access to high photon irradiances $2P/(\pi\omega_0^2)$ up to 555 mW cm^{-2}, the optical absorption of laser light within the band gap of the NCs and HNCs promotes the formation of a high quantity of electron-hole pairs so that the unavoidable trapping of carriers by bulk and surface defects becomes negligible. The number of photogenerated electrons that do not recombine with holes can be made large enough to reduce significantly Au^{3+} to metallic Au^0 NDs ($Au^{3+} + 3e^- \rightarrow Au^0$) on the surface of $Cu_{2-x}S$ NCs and $Cu_{2-x}S/CuInS_2$ short HNCs. In the meantime, the photogenerated holes react with the MeOH in solution.[40,46] This hole scavenger is compulsory since when no MeOH is added (Figure S1a, Supporting Information), we observe no Au metal deposition on the $Cu_{2-x}S$ NCs, nor on the short $Cu_{2-x}S/CuInS_2$ HNCs. The swift electron consumption leads to the rapid growth of a single Au ND, and the reaction almost reaches completion in less than 10 min exposure at the used laser intensities. Indeed, as shown in **Figure 2**a for both pure $Cu_{2-x}S$ NCs and short HNCs, tiny Au NDs with an average size of ≈5 nm are formed in the first minute, and their size further increases to ≈7 and ≈9 nm in 8 min (Figure 2b), to finally reach a marked plateau (Figure 2c,d) associated with the completion.

Figure 2e quantitatively shows the growth laws of a single Au ND on both pure $Cu_{2-x}S$ NCs and short HNCs. Interestingly, most of the Au NDs grown on the decorated disk-shaped $Cu_{2-x}S$ NCs did not nucleate on the disk surface but rather on the side. This observation indicates a higher density of activation sites at this location, likely attributed to lower protection by surface ligands in this zone. For short $Cu_{2-x}S/CuInS_2$ HNCs, the Au ND systematically deposits on the $Cu_{2-x}S$ side of the HNCs. In addition, TEM tracking shows that both the growth rate (variation of the gold ND size with time) and final size of Au NDs on short $Cu_{2-x}S/CuInS_2$ HNCs are distinctly bigger than those obtained on $Cu_{2-x}S$ NCs (Figure 2e).

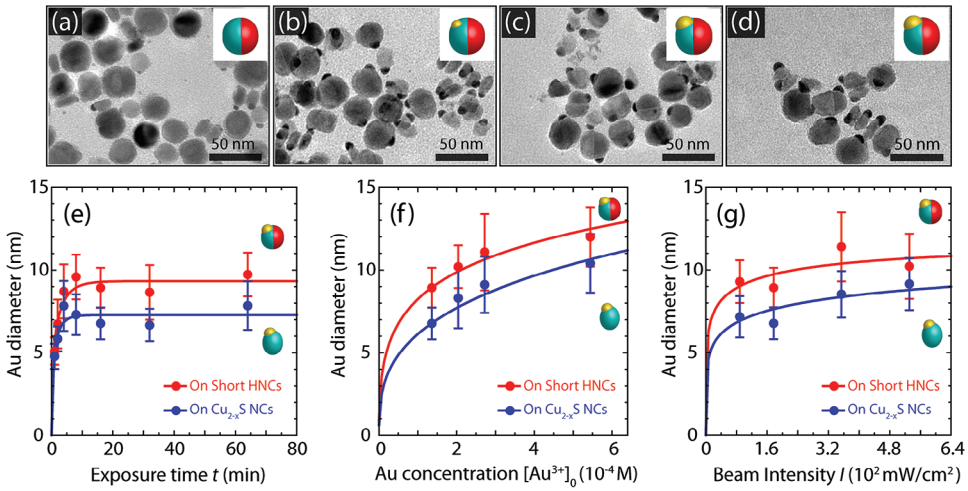

Figure 2. a–d) TEM images of a mixture of Au-$Cu_{2-x}S$ NCs (nanodisks lying flat or on the edge) and Au-$Cu_{2-x}S/CuInS_2$ HNCs (heterodimers showing an internal interface) obtained under different laser exposure times: a) 1 min; b) 8 min; c) 16 min; d) 64 min. Insets illustrate the temporal evolution of the gold size. e–g) Size variation of the Au NDs photodeposited on the short $Cu_{2-x}S/CuInS_2$ HNCs and $Cu_{2-x}S$ NCs with different photodeposition conditions: e) with laser exposure time (t); f) with concentration of Au^{3+} precursor ($[Au^{3+}]_0$); g) with the incident light intensity (I). The volume percentage of MeOH is 15%, the nanocrystal concentration is 1.068×10^{-8} M (2/3 [HNC], 1/3 [NC]), and when fixed, the exposure time t, the concentration $[Au^{3+}]_0$ and the beam power at the laser head P_L are kept at 8 min, 0.136 mM, and 100 mW, respectively; see the modeling section below for fit explanations.

We further investigated the influence of the hole scavenger (MeOH), time exposure, Au precursor concentration, and laser intensity. With no MeOH, we did not see the Au metal deposition on the $Cu_{2-x}S$ NCs nor on the short $Cu_{2-x}S/CuInS_2$ HNCs (Figure S1a, Supporting Information). With increasing MeOH concentration, the yields (Y) of Janus-based $Cu_{2-x}S$ NCs and $Cu_{2-x}S/CuInS_2$ HNCs decorated with a single Au ND increased drastically and reached a maximum of 81% at 15% MeOH (Figure S1b, Supporting Information). A further increase in the amount of MeOH did not improve the yield in single Au-decorated short HNCs/$Cu_{2-x}S$ NCs, likely related to the balance between hole scavenging and the number of electrons used for the photoreduction of gold ions (Figure S1c, Supporting Information). To study the influence of the light intensity on laser photodeposition, we then chose a set of conditions (MeOH 15%, reaction time t = 32 min, $[KAuCl_4]$ = 0.204 mM) and compared the formation of the gold ND in the dark and the presence of laser light (Figure S1d,e, Supporting Information). In the presence of photo-excitation, Au NDs could nucleate and grow very efficiently, while no Au ND formed in dark conditions.

The variation of the photodeposition yields (Y) over time (Figure S2, Supporting Information) shows that the yields of $Cu_{2-x}S$ NCs and $Cu_{2-x}S/CuInS_2$ HNCs decorated with a single Au ND increase drastically within the first 8 min to reach $Y >$ 95% and $Y >$ 85% respectively (15% MeOH). The Au photodeposition rate is higher on $Cu_{2-x}S/CuInS_2$ HNCs than on single-component $Cu_{2-x}S$ NCs (Figure 2e).

The precursor concentration ($[Au^{3+}]_0$) was also studied while setting the volume percentage of MeOH to 15%. The size of Au NDs deposited on either NCs increased with the $[Au^{3+}]_0$ (Figure S3, Supporting Information). Figure 2f illustrates quantitatively this variation, with again a higher growth rate and bigger final size of Au NDs on HNCs than those observed on pure $Cu_{2-x}S$ NCs; note that the yields (Y) of single Au-decorated short HNCs or $Cu_{2-x}S$ NCs also increase with $[Au^{3+}]_0$ and reach an asymptotic value of ≈ 95% at $[Au^{3+}]_0 = 2.04 \times 10^{-4}$ M after an exposure time of 16 min (Figure S3e, Supporting Information). We finally investigated the influence of the laser beam intensity inside the reaction cuvette (from 28 to 420 mW cm^{-2}) while all the other parameters remained the same (Figure S4, Supporting Information). The size of Au NDs on HNCs and $Cu_{2-x}S$ NCs gradually increased with the beam intensity and reached diameters of 9.5 and 8.5 nm respectively, at completion (Figure 2g). As already observed for $[Au^{3+}]_0$ and exposure time variations, the growth rate and final size of Au NDs on HNCs are higher than those on $Cu_{2-x}S$ NCs, again confirming that the photodeposition of Au NDs is more favorable on these HNCs than on pure $Cu_{2-x}S$ NCs. These robust behaviors in exposure time, gold ion concentration, and beam intensity, strongly support the conclusion that the $Cu_{2-x}S/CuInS_2$ Janus-type structure is more efficient in enhancing charge separation than the single-component $Cu_{2-x}S$ NCs. They also show that the photodeposition of Au NDs systematically takes place on $Cu_{2-x}S$, even in the presence of $CuInS_2$, for short HNCs.

2.2. Laser-Induced Au Photodeposition on Long $Cu_{2-x}S/CuInS_2$ HNCs

We carried out similar experiments using long $Cu_{2-x}S/CuInS_2$ HNCs to explore the robustness and versatility of this laser deposition technique. We performed TEM measurements at different exposure times while all the other parameters were kept the same (10% vol. MeOH, P_L = 100 mW, and $[Au^{3+}]_0$ = 0.204 mM). Within a very short exposure time (≈1 min), a tiny single Au ND (≈5 nm) nucleated and grew on the $Cu_{2-x}S$ tip of the long HNCs (**Figure 3a**), and its size increased with exposure time (Figure 3b). Interestingly, as opposed to what is observed for short $Cu_{2-x}S/CuInS_2$ HNCs, secondary nucleation and growth of Au ND also occurred, after some delay, on the side of the $CuInS_2$

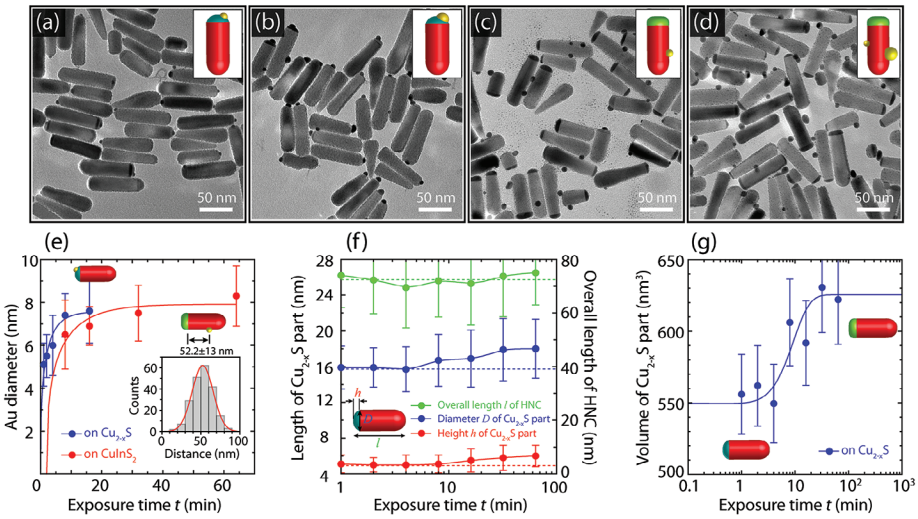

Figure 3. a–d) TEM images of gold ND deposition on long $Cu_{2-x}S/CuInS_2$ HNCs obtained for different laser exposure times: a) 1 min; b) 8 min; c) 16 min; d) 64 min). Insets illustrate the morphology evolution of these HNCs in time (color code: yellow for Au NDs, cyan for $Cu_{2-x}S$, green for Au-$Cu_{2-x}S$, red for $CuInS_2$); e) Size evolution of Au NDs photodeposited on $Cu_{2-x}S$ tips and on the side of elongated $CuInS_2$ rods for different laser exposure times (see modeling section below for the fit explanation). Inset: distribution histogram of the distance between the hetero-interface of $Cu_{2-x}S/CuInS_2$ and the first Au ND nucleated on the elongated side of the $CuInS_2$ part. The histogram was constructed by measuring over 200 HNCs obtained for an exposure time of 16 min., i.e., for the sample illustrated in (c); it is well-fitted with a single Gaussian profile. f) Variation of the maximum diameter D (blue dots, left Y-axis) and height h (red dots, left Y-axis) of the $Cu_{2-x}S$ part, and of the average overall length l of the HNCs (green dots, right Y-axis) with deposition time. g) Variation of the global volume of the $Cu_{2-x}S$ tips in HNCs as a function of exposure time when assuming a spherical cap shape (see text and modeling section for the fit explanation); each data is obtained by measuring the size of $Cu_{2-x}S$ tips over a hundred single gold deposited HNCs without considering the volume of the initial Au ND. The volume percentage of MeOH, power at laser exit, and laser exposure time are 10%, 100 mW, and 16 min, respectively.

segment (Figure 3c). The measured average contact angle of Au NDs on the $CuInS_2$ segment is almost $\bar{\theta} \approx 180°$ (Figure 3a–d), as already observed on CdS wurtzite-type nanostructures,[46] while $\bar{\theta} \approx 90°$ on the $Cu_{2-x}S$ tips (see below). Moreover, by contrast to the observations made on short $Cu_{2-x}S/CuInS_2$ HNCs, the Au NDs deposited on the $Cu_{2-x}S$ tips at short irradiation time seem to disappear progressively with a concomitant sharp increase of the contrast of the $Cu_{2-x}S$ part as compared to the $CuInS_2$ one (Figure 3c). This observation indicates that the composition of the Au-$Cu_{2-x}S$ part of the HNCs is modified with a possible inter-diffusion/reaction of the already deposited gold with the $Cu_{2-x}S$ part. Typically, for an exposure time longer than 16 min, no more Au NDs were found on the $Cu_{2-x}S$ tips. A new photodeposition event took place on the side of the elongated $CuInS_2$ part (Figure 3d). The growth of Au NDs on the two $Cu_{2-x}S$ and $CuInS_2$ parts is illustrated in Figure 3e. In the first step, the Au ND grows on the $Cu_{2-x}S$ portion and reaches a maximum diameter of ≈ 8 nm. In a second step it progressively vanishes, while at the same time, the nucleation and growth of an additional Au ND on the $CuInS_2$ portion (see Figure 3c) takes place. Tracking the photodeposition process, thus, indicates that the nucleation and growth of Au NDs on the long $Cu_{2-x}S/CuInS_2$ HNCs proceed in sequential steps, i.e., the selective deposition of a metallic Au ND on the $Cu_{2-x}S$ tip followed by a delayed growth of an Au ND on the side of elongated $CuInS_2$ segment.

Concomitantly, the contrast of the $Cu_{2-x}S$ tips on the TEM images gradually increases (Figure 3c,d). This observation suggests that the Au-$Cu_{2-x}S$ part in HNCs experiences a change in composition by incorporating Au^+ into $Cu_{2-x}S$ and forming Au_2S areas (evidenced by HRTEM, see Section 5). Since this transformation occurs in the presence of an already photodeposited Au ND and continuous light excitation, the reaction involved cannot be a simple cation exchange,[6,47,48] which should have already been at work on short HNCs and in the dark, by contrast to our experimental observations. Therefore, we propose a photo-activated mechanism only triggered on long HNCs (see the modeling section below). As the transformation of $Cu_{2-x}S$ into Au_2S is known to increase the unit volume of the crystal lattice, such incorporation of Au^+ in $Cu_{2-x}S$ is illustrated by the variation of both diameter $D(t)$ and height $h(t)$ of the $Cu_{2-x}S$ tips with the exposure time (Figure 3f). The corresponding variation of the volume is thus given by $V(t) = \frac{\pi}{6} h(t)(\frac{3}{4}D(t)^2 + h(t)^2) - \frac{\pi D_0^2}{4}(h(t) - h_0)$, assuming a spherical cap shape, and subtracting the volume of $CuInS_2$ possibly covered by the expanding Au-$Cu_{2-x}S$ tip as suggested by the constant overall length l of the long HNCs. This volume increase is quite significant (≈ 15%) as illustrated in Figure 3g. Moreover, when deposited on the elongated part of $CuInS_2$, Au NDs are located on the side, in sharp contrast to Au photodeposition on Cd chalcogenide nanorods typically taking place at the tip.[41,46,49,50] Furthermore, the distance distribution of the Au ND location on the side of elongated $CuInS_2$, measured from the hetero-interface of $Cu_{2-x}S/CuInS_2$, follows a single Gaussian profile with an average distance of ≈ 52 nm and a deviation of ≈ 25% (see Inset of Figure 3e). This nearly constant value is likely regulated by the spatial distribution of the photogenerated free electrons that can reduce Au^{3+} to metallic Au NDs. This may be related to a competition between the rate of electron capture by gold reduction on the side of the long $CuInS_2$, impossible for short ones, and the

rate of electron transfer at the Janus-like $Cu_{2-x}S/CuInS_2$ heterointerfaces. Finally, Figure 3d shows that in some cases, the nucleation and growth of a second Au ND on the elongated $CuInS_2$ side may appear at very late stages. This could be explained by the near absence of wetting of the Au NDs on $CuInS_2$ (mean contact angle close to $\bar{\theta} \approx 180°$, see Figure 3c); the decreasing ratio of the contact area to the surface of a growing Au ND progressively reduces the electron transfer and eventually makes it insufficient to sustain Au ND growth. The resulting accumulation of photogenerated electrons in the $CuInS_2$ thus triggers the nucleation of a new Au ND.

As with short $Cu_{2-x}S/CuInS_2$ HNCs, the photodeposition of Au NDs on long $Cu_{2-x}S/CuInS_2$ HNCs is also governed by reaction parameters such as the concentration of hole scavenger and gold precursor, and the laser intensity. As shown in Figure S5 (Supporting Information) for $[Au^{3+}]_0 = 0.204$ mM and $P_L = 100$ mW, the photodeposition yield (Y) significantly increases once at least a 10% volume MeOH is used to ensure charge transfer equilibration and reaches a maximum of 70% after an exposure of 32 min. Moreover, the size of the photodeposited Au ND on the $CuInS_2$ side increases from 6.8 ± 1.1 nm to 7.5 ± 1.2 nm when the addition of MeOH goes from 5% to 15%, again confirming its crucial role in hole scavenging and charge balancing in the photodeposition process.

In the same way, we showed that the growth of Au NDs on the long $Cu_{2-x}S/CuInS_2$ HNCs could also be controlled by the laser beam intensity using an optimized methanol concentration of 10%, the same concentration of gold ions $[Au^{3+}]_0 = 0.204$ mM and an exposure time of 16 min (Figures S6 and S7, Supporting Information). The gold ND size variation with the beam power (Figure S7a, Supporting Information) and the gold ND distribution between the two portions of the HNCs (Figure S7c, Supporting Information) confirm that 20% of the Au NDs grown on the $Cu_{2-x}S$ side are still present after 16 min irradiation and have a maximum size of 7.6 ± 1.5 nm for P_L up to 100 mW; then, they disappear with a further increase in power. Conversely, by varying the beam power between 20 to 300 mW, the size of the Au NDs on the $CuInS_2$ portion increases gradually from 5.8 ± 0.9 nm to 7.6 ± 1.2 nm (Figures S6 and S7, Supporting Information). Moreover, the yield (Y) in HNCs decorated with single Au NDs decreases from 78% to 66%, while that of HNCs decorated with multiple Au NDs goes from 0 to 8% (Figure S7b,c, Supporting Information). The overall length l of the HNCs does not vary with power (Figure S8a, Supporting Information), while the diameter D of $Cu_{2-x}S$ and its height h increase slowly (Figure S8b, Supporting Information), as already observed with exposure time experiments (Figure 3f). These data suggest that the dynamic changes in the composition of the growing Au-$Cu_{2-x}S$ portions promote spreading and eventually outflank the $CuInS_2$ portion, forming a sort of lip on its surface (see Figure 3d).

Finally, the control of the Au ND growth was further performed by tuning the Au^{3+} precursor concentration, while the other parameters were kept identical and constant (10% vol. MeOH, $P_L = 100$ mW, and exposure time of 16 min). TEM images in Figure S9 (Supporting Information) clearly show that the size of Au NDs increases with $[Au^{3+}]_0$. At low $[Au^{3+}]_0$, most Au NDs (6.3 ± 1.4 nm) grow on the $Cu_{2-x}S$ part of the HNCs (Figure S10a—c, Supporting Information), with no additional growth observed on the $CuInS_2$ segment. For $[Au^{3+}]_0 = 0.136$ mM, Figures S9b and S10c (Supporting Information) show that Au ND deposition statistically occurs on either side of the Janus structure with almost equal probability (52% on $Cu_{2-x}S$ par and 48% on $CuInS_2$ part. With a further increase of $[Au^{3+}]_0$, nearly no individual Au ND is observable on the $Cu_{2-x}S$ part; almost all of them are on the $CuInS_2$ side, (average size of ≈ 7.5 nm) (Figures S9c,d, and S10a, Supporting Information). Additionally, once again, the contrast of the $Cu_{2-x}S$ part became darker compared to that of the starting $Cu_{2-x}S/CuInS_2$ HNCs (Figure S9, Supporting Information), and the size of this $Cu_{2-x}S$ zone increased slightly (Figure S11, Supporting Information), as already observed when varying the exposure time and the beam power. These observations again confirmed a continuous evolution in the composition of the Au-$Cu_{2-x}S$ domains, Au_2S being the most probable candidate according to experiments triggered by electron beams.[51]

2.3. Structural Characterization of Au-$Cu_{2-x}S/CuInS_2$ Hybrid Long HNCs

To reveal the underlying mechanisms in the selective photodeposition of Au NDs on the $Cu_{2-x}S/CuInS_2$ HNCs, high-resolution TEM images of the Janus-like Au-$Cu_{2-x}S/CuInS_2$ HNCs obtained after different exposure times were performed. As demonstrated in **Figure 4a**, before photodeposition, we observe the $Cu_{2-x}S$ part (blue square) of the HNCs with its monoclinic low chalcocite crystal structure (JCPDS file n° 31–0482), and the elongated $CuInS_2$ portion of the rod (red square) with the hexagonal wurtzite crystal structure (JCPDS file n° 47–1372), consistent with previous reports.[22,39]

Then, during the first photodeposition step (≈ 8 min), a small single ND of ≈7 nm, is successfully deposited on the $Cu_{2-x}S$ tip. These individual NDs are crystalline with a crystal lattice d-spacing of ≈ 0.2 nm, which can be indexed to the (200) plane of cubic Au crystals (Figure 4). Interestingly, when photodeposition is held for several minutes longer, the gradual disappearance of the Au NDs on the $Cu_{2-x}S$ tips, accompanied by an obvious stronger contrast as mentioned above, corresponds to an increase in the d-spacing of the crystal lattice from 0.34 to 0.38 nm (Figure 4c), confirming the already hypothesized non-negligible change in the composition of the $Cu_{2-x}S$ tips. Indeed, a close look at the $Cu_{2-x}S$ tips reveals the presence of a new lattice fringe with a d-spacing of 0.29 nm, which can be indexed to the (111) plane of Au_2S (Figure 4c,d), and thus strongly suggests the incorporation of gold atoms into $Cu_{2-x}S$ structure. At an exposure time of ≈ 32 min, we also observe the Au NDs photodeposited on the elongated side of the $CuInS_2$ parts (Figure 4d) that show the distinct lattice spacing of 0.24 nm indexed to the (111) facets of cubic Au crystals.

This composition of the Au_2S-$Cu_{2-x}S$ tips on long HNCs is described by STEM images and a 2D elemental mapping, as shown in Figures S12 and S13 (Supporting Information). Figure S12 (Supporting Information) illustrates a sample where a few short HNCs are still present in a large assembly of long ones to compare the differences as well in behavior between short and long HNCs in the same experiment. Before any electron beam exposure, the Au-containing $Cu_{2-x}S$ tips of long HNCs exhibit a black homogeneous contrast (Figure S12a, Supporting Information, blue arrows) compared to the elongated $CuInS_2$ segments while

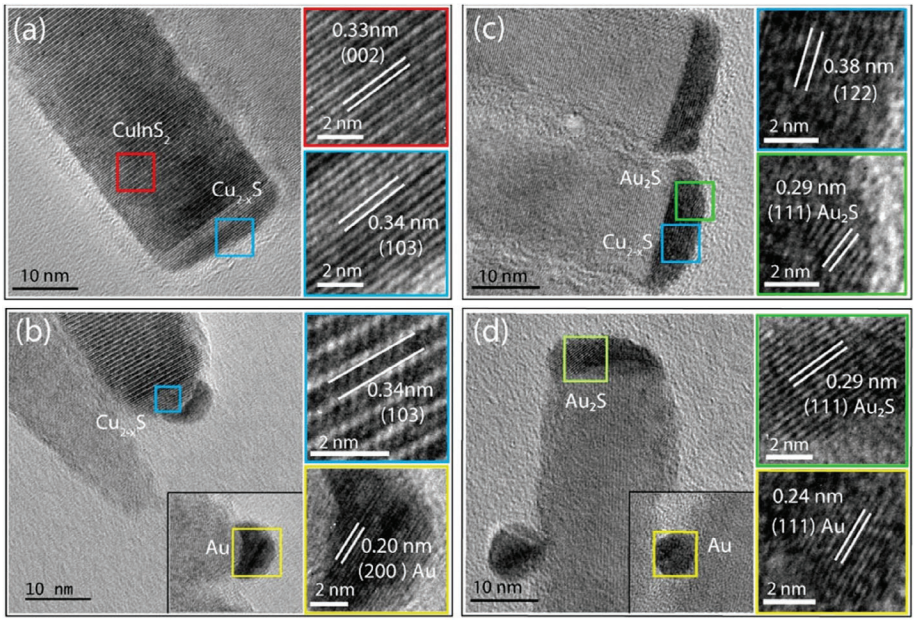

Figure 4. a) High-resolution TEM image of long $Cu_{2-x}S/CuInS_2$ HNCs. The $Cu_{2-x}S$ tip (blue square) and elongated $CuInS_2$ rod (red square) can be indexed to monoclinic low chalcocite and hexagonal wurtzite crystal structures, respectively. b) High-resolution TEM image of Au-$Cu_{2-x}S/CuInS_2$ hybrid HNCs after 8 min laser exposure (P_L = 100 mW and 10% vol. MeOH). Single NDs are deposited on the side of $Cu_{2-x}S$ tips (yellow square). The crystal lattice d-spacing of the NDs matches well with the (200) plane of cubic Au nanoparticles (JCPDS file n° 04–0784). c) High-resolution TEM of Au-$Cu_{2-x}S/CuInS_2$ hybrid HNCs after 16 min laser exposure (P_L = 100 mW and 10% vol. MeOH). The Au NDs on the $Cu_{2-x}S$ side disappear while the contrast and d-spacing (blue square) of the $Cu_{2-x}S$ tips increase. The crystal lattice d-spacing of some part (green square) of the $Cu_{2-x}S$ tip matches well with the (111) plane of cubic Au_2S (JCPDS file n° 085–1997). d) High-resolution TEM of Au-$Cu_{2-x}S/CuInS_2$ hybrid HNCs after 32 min laser exposure (P_L = 100 mW and 10% vol. MeOH). An extra Au ND (yellow square) has nucleated on the side of the elongated $CuInS_2$ part, and its crystal lattice d-spacing matches well with the (111) plane of cubic Au nanoparticles.

short HNCs exhibit a well-defined Au ND on top of the $Cu_{2-x}S$ part (Figure S12a, Supporting Information, green arrows). However, long HNCs suffer from staying below the electron beam, and after 8 min of exposure, the initial flat surface of the same Au-containing $Cu_{2-x}S$ part becomes irregular with the formation of two separated areas (Figure S12b, Supporting Information, yellow arrows). This result can be attributed to the reduction of Au^+ from Au_2S to Au^0 by the electron beam and a subsequent structural re-arrangement in the form of phase separation with metal Au leaking out from the Au_2S-$Cu_{2-x}S$ tips; Au_2S can indeed be metastable and readily reduced to metal Au under illumination by an electron beam (yellow arrows, Figure S12b, 8 min electron beam exposure, and dynamically Figure S12c up to 15 min, Supporting Information).[47,51] This poor stability of Au-containing $Cu_{2-x}S$ tips under electron beam illumination makes the identification of their structure and composition extremely challenging. After the Au metal leakage from $Cu_{2-x}S$ tips, the interface between the two $Cu_{2-x}S$ and $CuInS_2$ portions is still visible, showing the contrast in the HNC composition (Figure S12b,c, Supporting Information). Conversely, small HNCs do not show any modification after electron beam exposure (red arrows, Figure S12b, Supporting Information), demonstrating that the formation of Au_2S is not detectable on the $Cu_{2-x}S$ part of the short HNCs, as suggested by the long-time stability of the Au NDs. Focusing on long HNCs, Figure S13 (Supporting Information) shows STEM images captured at the beginning of the scan and after an 8-min scan and the corresponding elemental mapping (Figure S13c–g, Supporting Information) of Au_2S-$Cu_{2-x}S/CuInS_2$ HNCs obtained after the Au ND deposited on $Cu_{2-x}S$ did disappear. As expected, the concomitant presence of S/Cu, Cu/In, and S/In is observed on the $CuInS_2$ fragment as well as that of the couple Au/Cu on the $Cu_{2-x}S$ part. The element that confirms the initial presence of gold all over the $Cu_{2-x}S$ part is the gold distribution profile *and* its asymmetry (Figure S13i,j, Supporting Information) along the line scan (Figure S13h, Supporting Information), which shows a continuous averaging between what is observed in STEM images and inversion in the copper and gold contents. The high-resolution TEM images shown in Figure 4c,d, and this structural characterization thus support the fact that Au^0 is oxidized under light excitation, to form Au_2S at the $Cu_{2-x}S$ part.

3. Kinetic Modeling and Comparison to Experiments

Single gold ND growth was described theoretically in previous investigations of laser deposition on TiO_2 NPs[40] and CdSe/CdS NRs.[46] Conceptually, we assume that gold NDs have a spherical cap shape and consider that their growth on an NC, well after the nucleation step, is triggered by a flux of gold atoms produced on the $Cu_{2-x}S$ or $CuInS_2$ surface due to the field gradient effect induced by, and directed toward this metal ND. Comparisons between experiments and models strongly support a reaction-limited mechanism.[40] Therefore, the total flux of gold atoms at the perimeter of the growing ND, $\Phi(t)$, is proportional to the photoproduction rate of gold atoms $d[Au^0]/dt$. On the one

hand, we have $\Phi(t) = [\nu_{Au}/(Y[NC])]\, d[Au^0]/dt$, where ν_{Au} is the volume of a gold atom, Y is the yield in single Au-decorated NCs, and thus $Y[NC]$ is the NC concentration on which the photodeposition takes place effectively. On the other hand, mass conservation dictates $\Phi(t) = dV/dt$, where $V(t)$ is the volume of the photodeposited gold ND. As the expression of $V(t)$ depends on the contact angle θ of the gold ND on the chosen NC, we systematically measured its height h and largest diameter D for all the experiments in which θ could be deduced; if $D/h > 2$ (resp. $D/h < 2$), then $\theta < 90°$ (resp. $\theta > 90°$), see Figure S14 (Supporting Information). Experiments show that the average measured values always satisfy $\bar{\theta} \geq 90°$: (i) $\bar{\theta} = 102°$ on $Cu_{2-x}S$ seeds, (ii) $\bar{\theta} = 88° \approx 90°$ on the $Cu_{2-x}S$ part of the short HNCs, (iii) $\bar{\theta}$ slightly decreases with growth time in the case of the Au ND growth on the $Cu_{2-x}S$ portion of long HNCs and reaches $\bar{\theta} = 91° \approx 90°$, (iv) $\bar{\theta}$ is close to 180° on the wurtzite $CuInS_2$ segment of long HNCs. Then, the volume $V(t)$ of Au ND can be estimated using $V(t) = \pi D(t)^3 \kappa(\theta)/8$, where $\kappa(\theta) = (2/3 - cos\theta + 1/3cos^3\theta)$.[52] Finally, the growth of single gold NDs onto the $Cu_{2-x}S$ or the $CuInS_2$ fragments is given by (Equation 1):

$$D^3(t) = \frac{8}{\pi\kappa(\theta)} \frac{\nu_{Au}}{Y[NC]} \left[Au^0\right](t) \tag{1}$$

where $t = 0$ s indicates the time when the laser exposure is turned on, $[Au^0](t = 0) = 0$, and when the critical nucleation diameter $D_c = D(t \approx 0)$ is neglected because we look at growth times high compared to the nucleation one. The following step, thus, requires a description of the photoreduction of Au^{3+} ions on the surface of the NCs.

3.1. Photodeposition Reaction Schemes

Early Stage, Gold ND Growth on $Cu_{2-x}S$. Based on the measurements of the mean contact angles we can assume that Au^{3+} presents a better affinity for $Cu_{2-x}S$ ($\bar{\theta} \approx 90°$) than for $CuInS_2$ surface ($90° \ll \bar{\theta} < 180°$), partly because $Cu_{2-x}S$ presents a deficit in positive charges. Therefore, we expect the following relation between the photoreduction rates of the gold ions $k_{e,i}^{Cu_{2-x}S} \gg k_e^{CuInS_2}$, where the subscript i = 'seeds', 'short HNCs', 'long HNCs' indicates the type of NCs. Then, the gold ND growth is always favored first on the $Cu_{2-x}S$ part. Charge balance is ensured by the presence of a hole scavenger, here methanol ($HS + h^+ \xrightarrow{k_{h,i}^{HS}} HS^+$). Moreover, as soon as a first gold ND nucleates on $Cu_{2-x}S$, it promotes charge separation[53] and rapidly generates, within the NC, an electric field gradient, which reinforces the attraction of electrons toward the Au-$Cu_{2-x}S$ portion and enhances ND growth. The first stage is thus described by (Equation 2):

$$\begin{cases} \left[NC_i + h\nu\,(> E_{bg,i}) \underset{k_{r,i}}{\overset{g_i}{\rightleftharpoons}} NC_i\,(e^-, h^+) \right]_{\text{bulk NC}} \\ \left[HS + h^+ \xrightarrow{k_{h,i}^{HS}} HS^+ \right]_{\text{surface NC}} \\ \left[Au^{3+} + 3e^- \xrightarrow{k_{e,i}^{Cu_{2-x}S}} Au^0 \right]_{\text{surface } Cu_{2-x}S} \end{cases} \tag{2}$$

For photon energies above the band gaps, $\hbar\omega > E_{bg,i}$, electrons and holes are produced in the bulk of NCs by optical absorption, with a production rate g_i; in the linear regime of optical excitation, we have $g_i = \frac{\sigma_{abs,i}[NC]I}{\hbar\omega}$, with $I \approx 2P/(\pi{\omega_0}^2)$ the beam intensity in the sample (P: beam power, $\omega_0 = 0.5\ cm$: beam waist), and $\sigma_{abs,i}$ the average NC absorption cross-section. They recombine with a bulk reaction rate $k_{r,i}$ while the oxidation of the hole scavenger on the NCs surface occurs at a rate $k_{h,i}^{HS}$, and the reduction of Au^{3+} at the surface of $Cu_{2-x}S$ is characterized by $k_{e,i}^{Cu_{2-x}S}$. Note that an extra photo-oxidation reaction $Au^0 + h^+ \xrightarrow{k_h^{Au^+}} Au^+$ on the already grown ND, and involved later on in the reaction scheme for long HNCs, cannot take place on the Au-$Cu_{2-x}S$ location of $Cu_{2-x}S$ seeds and short HNCs due to the strong field gradient effect that efficiently pushes positive charges away from the Au ND. Concomitantly, the $CuInS_2$ part of short HNCs becomes very electron-poor, and the growth of second Au ND by photoreduction of gold ions cannot occur on this part, as experimentally observed.

Late Stage, Gold ND Growth on $CuInS_2$. Conversely, even if the number of carriers produced increases with the size of the HNCs, leading to the observation of higher Au ND growth rates on long HNCs as compared to $Cu_{2-x}S$ seeds and short HNCs (see below), the induced field gradient drastically decreases (by at least a factor $\approx l_{Long\ HNC}/l_{Short\ HNC} \approx 5$ using a simple geometric argument) so that the charge separation is much less pronounced. Then, many electrons remain available on the $CuInS_2$ part of long HNCs to possibly trigger the nucleation and growth of a second gold ND at a late stage through the photoreduction of Au^{3+}. If so, charge balancing may switch part of the hole consumption from the main scavenging methanol reaction $HS + h^+ \xrightarrow{k_{h,i}^{HS}} HS^+$ to the oxidation of gold NDs first deposited on $Cu_{2-x}S$, $Au^0 + h^+ \xrightarrow{k_h^{Au^+}} Au^+$, and thus now concomitantly promotes the formation of Au_2S areas in the Au-$Cu_{2-x}S$ part. This second step scenario for long HNCs, coherent with experimental observations and characterizations, is described by (Equation 3):

$$\begin{cases} \text{carrier production} \left[HNC + h\nu\,(> E_{bg}) \underset{k_r}{\overset{g}{\rightleftharpoons}} HNC\,(e^-, h^+) \right]_{\text{bulk NC}} \\ e^- \text{ consumption} \left[Au^{3+} + 3e^- \xrightarrow{k_e^{CuInS_2}} Au^0 \right]_{\text{surface } CuInS_2} \\ h^+ \text{ consumption} \begin{cases} \left[HS + h^+ \xrightarrow{k_{h,i}^{HS}} HS^+ \right]_{\text{surface NC}} \\ \left[Au^0 + h^+ \xrightarrow{k_h^{Au^+}} Au^+ \right]_{\text{bulk Au/Cu}_{2-x}S} \end{cases} \\ \begin{cases} \text{Cu}_{2-x}\text{S vacancy filling} \left[2Au^+ + S^{2-} \xrightarrow{k_{Au_2S}} Au_2S \right]_{\text{bulk Au/Cu}_{2-x}S} \\ \text{Cation exchange} \left[Cu_{2-x}S + 2Au^+ \xrightarrow{k_{AuCu}} Au_2S + 2Cu^+ \right]_{\text{bulk Au/Cu}_{2-x}S} \end{cases} \end{cases} \tag{3}$$

where $k_h^{Au^+}$ is the oxidation rate of Au^0, k_{Au_2S} is the reaction rate to form Au_2S by filling vacancies of $Cu_{2-x}S$, and k_{AuCu} is the reaction rate for cation exchange between Cu^+ and Au^+; it was indeed demonstrated that the two mechanisms could be simultaneously triggered together.[51] To solve these equations, we make the following assumptions: i) we neglect the carrier diffusion within NCs because the equilibration time of carrier concentrations is short compared to any photodeposition growth time scale, ii) methanol is always in excess in the experiments so that $[HS](t) \approx [HS]_0$ and, iii) the photoreduction of Au^{3+} is assumed to be pseudo-first-order.

3.2. Early Growth of Gold NDs on $Cu_{2-x}S$ Seeds, and $Cu_{2-x}S$ Tips of Short and Long HNCs

Early Growth of Gold NDs Modeling on $Cu_{2-x}S$. The Au^0 production to grow a gold ND on the surface of $Cu_{2-x}S$ is thus expected to be described by (Equation 4):

$$\begin{cases} \frac{d[e]_i}{dt} = \left(g_i - k_{r,i}[e]_i[h]_i\right)_{\text{bulk NC}} - \left(k_{e,i}^{Cu_{2-x}S}[e]_i\left[Au^{3+}\right]\right)_{\text{ads } Cu_{2-x}S} \\ \frac{d[h]_i}{dt} = \left(g_i - k_{r,i}[e]_i[h]_i\right)_{\text{bulk NC}} - \left(k_{h,i}^{HS}[h]_i[HS]\right)_{\text{ads NC}} \\ \frac{d[HS^+]}{dt} = \left(k_{h,i}^{HS}[h]_i[HS]\right)_{\text{ads NC}} \\ \frac{d[Au^0]}{dt} = -\frac{d[Au^{3+}]}{dt} = \left(k_{e,i}^{Cu_{2-x}S}[e]_i\left[Au^{3+}\right]\right)_{\text{ads } Cu_{2-x}S} \end{cases} \quad (4)$$

where the subscript i = 'seeds', 'short HNCs', 'long HNCs' indicates the type of NCs. The detailed resolution of this set of equations is given in SI, (SI 15). The main stages to determine $[Au^0](t)$ involved in the gold ND growth (Equation 1), are as follows:

i) The NCs are covered by stabilizing ligands (dodecanethiol, DDT), and gold ions $AuCl_4^-$ are solubilized in toluene using solubilizing agents (dodecylamine, DDA). So, the adsorbed concentrations $[Au^{3+}]_{ads,i}$ and $[HS]_{ads,i}$, which react with the electrons and holes produced by laser absorption, are assumed to be simply related to their bulk values $[Au^{3+}]_{ads,i} \approx C_{Au,i}[Au^{3+}]$ and $[HS]_{ads,i} \approx C_{HS,i}[HS]$, where the proportionality constants, $C_{Au,i}$ and $C_{HS,i}$ depend on the type of NCs, the ligands, and the stabilizing agents.[54]

ii) We consider the charge balance at growth time scales, $d[e]_i/dt = d[h]_i/dt$, from which we determine the stationary electron concentration $[e]_{sta,i} = \sqrt{\frac{k_{h,i}^{HS}[HS]_{ads,\,i}\cdot g_i}{k_{r,i}k_{e,i}^{Cu_{2-x}S}[Au^{3+}]_{ads,i}}}$ under the high-field excitation condition associated with focused lasers ($\frac{k_{r,i}}{k_{h,i}^{HS}[HS]_{ads,\,i}}[e]_i \gg 1$).

iii) $[e]_{sta,i}$ is further introduced into the rate equation $\frac{d[Au^{3+}]}{dt} \approx -k_{e,i}^{Cu_{2-x}S}[e]_{sta,i}[Au^{3+}]_{ads,i}$. The solution is: $[Au^{3+}]\ (t \le 2(\tau_e)_i) = \beta_i\ [Au^{3+}]_0\left(1 - \frac{t}{2(\tau_e)_i}\right)^2$ where, $\beta_i[Au^{3+}]_0$ is the maximum amount of Au^{3+} that is effectively deposited on the type of NCs in the presence of ligands ($\beta_i \le 1$) and, $(\tau_e)_i = \sqrt{\frac{k_{r,i}\beta_i[Au^{3+}]_0}{k_{e,i}^{Cu_{2-x}S}k_{h,i}^{HS}C_{Au,i}C_{HS,i}[HS]_0\cdot g_i}}$ is the time scale for the gold ions photoreduction. Accordingly, we get (Equation 5):

$$\left[Au^0\right]\ \left(t \le 2(\tau_e)_i\right) = \beta_i\left[Au^{3+}\right]_0 \cdot \frac{t}{(\tau_e)_i} \cdot \left|1 - \frac{t}{4(\tau_e)_i}\right| \quad (5)$$

iv) Eventually, using (Equation 1), the growth law of the gold ND onto the $Cu_{2-x}S$ part is given by (Equation 6):

$$Y_i[NC]_i V_i\ \left(t \le 2(\tau_e)_i\right) = \nu_{Au}\,\beta_i\left[Au^{3+}\right]_0 \frac{t}{(\tau_e)_i} \cdot \left|1 - \frac{t}{4(\tau_e)_i}\right| \quad (6)$$

where $V_i = \pi D_i^3\kappa(\theta)/8$ is the volume of the gold ND; this behavior is followed by an exponential saturation toward completion.[46] The gold ND growth is thus described by: $\frac{Y_i[NC]_i}{[Au^{3+}]_0}D_i(t/(\tau_e)_i)^3 \approx f(t/(\tau_e)_i)$, indicating how data obtained in various conditions can be rescaled all together in amplitude and time scale to raise a single master behavior; the function f is essentially given by the temporal behavior of (Equation 6).

Early Growth of Gold NDs on $Cu_{2-x}S$, Data Analysis. **Figure 5** shows plots of the overall set of measurements performed under all the different conditions (variations in exposure time t, $[Au^{3+}]_0$ concentration, and beam intensity I) in the rescaled form $D_i[\frac{Y_i[NC]_i}{[Au^{3+}]_0}]^{1/3}$ as a function of $t/(\tau_e)_i \propto \sqrt{[NC]_i \cdot I/[Au^{3+}]_0}\cdot t$ for $Cu_{2-x}S$ seeds (Figure 5a), and $Cu_{2-x}S$ portion of short (Figure 5b) and long HNCs (Figure 5c). We observe the collapse of the different data onto single master behaviors predicted by the growth modeling over more than one order of magnitude in rescaled time for the growth of gold NDs on any type of $Cu_{2-x}S$ NC, whether they are seeds or short/long HNCs. Moreover, we can deduct from all these fits, the gold ND diameters at completion: $D_{\infty,Seed} = 0.19[\frac{[Au^{3+}]_0}{Y\cdot[Seed]}]^{1/3}$ nm, $D_{\infty,Short\ HNC} = 0.30[\frac{[Au^{3+}]_0}{Y\cdot[Short\ HNC]}]^{1/3}$ nm and $D_{\infty,Long\ HNC} = 0.17[\frac{[Au^{3+}]_0}{Y\cdot[Long\ HNC]}]^{1/3}$ nm.

Considering (Equation 6), based on i) the measured contact angles for the determination of $\kappa(\theta)$, respectively $\bar{\theta} = 102°$ on $Cu_{2-x}S$ seeds, and $\bar{\theta} \approx 90°$ on the $Cu_{2-x}S$ portion on both short and long HNCs, ii) the mean experimental deposition yields, respectively $\bar{Y}_{Seed} = 98\%$, $\bar{Y}_{Short\ HNC} = 86\%$ and $\bar{Y}_{Long\ HNC} = 70\%$ and, iii) the atomic volume of gold $\nu_{Au} = M_{Au}/(N_A\varrho_{Au})$, where $M_{Au} = 196.97$ g is the molar mass, $\rho_{Au} = 19.3$ g cm^{-3} is the density and N_A is Avogadro's number, we find $\beta_{Seed} = (14.45 \pm 1.41)\%$ and $\beta_{Short\ HNC} = (41.75 \pm 4.34)\%$ for the experiments performed in a mixture composed of seeds (1/3) and short HNCs (2/3), so that the global percentage of gold ions deposited at completion is $\beta_{Seed} + \beta_{Short\ HNC} \approx 56\%$. On the other hand, we find $\beta_{Long\ HNC} = (7.11 \pm 0.42)\%$, which is quite low, likely because a second growth stage (and even a third one) emerges later on the $CuInS_2$ part of the long HNCs (see below); errors in β are deduced from the

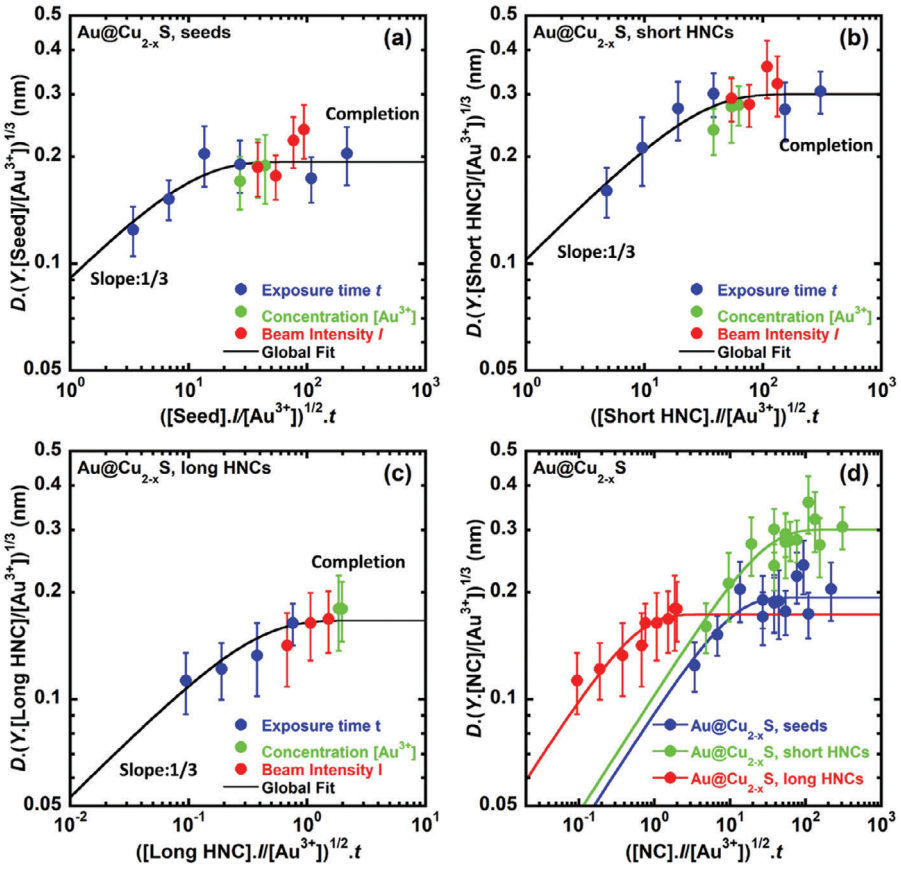

Figure 5. Plots of the single gold ND diameter growth $D_i \cdot (Y_i[\mathrm{NC}]_i/[\mathrm{Au}^{3+}]_0)^{1/3}$ rescaled as a function of the rescaled time $t/(\tau_e)_i \propto \sqrt{[\mathrm{NC}]_i \cdot I/[\mathrm{Au}^{3+}]_0} \cdot t$ (subscript i indicating either seeds, short or long HNCs) onto $Cu_{2-x}S$ for a) seeds, b) short HNCs, c) long HNCs, when varying the exposure time t, the initial gold ion concentration $[\mathrm{Au}^{3+}]_0$ and the beam intensity I, all the other parameters being fixed. The fitting curve is composed of two successive behaviors, the early one predicted by (Equation 6), followed by an exponential saturation in $t/(\tau_e)_i$ until the completion of the photoreaction in the finite volume of the solution (1 cm^3). d) Comparison between the three rescaled dynamics a–c) showing the influence of the increasing size of the $CuInS_2$ portion on the gold ND growth rate. The error in the ND diameter corresponds to the standard deviation obtained on at least 200 measurements.

standard deviation of the set of fits. Comparing the three rescaled dynamics together (Figure 5d), we note the strong influence of the presence of the $CuInS_2$ portion on the growth of Au ND: the longer the $CuInS_2$ segment, the higher the early growth rate of the Au ND on $Cu_{2-x}S$. Thus, the modeling does predict the first stage of gold deposition on $Cu_{2-x}S$, and the overall data rescaling allows for the rationalization and sorting of the different growth rates: $Cu_{2-x}S$ NC < Short HNC < Long HNC. This sorting in growth rates on $Cu_{2-x}S$ could be explained by the fact that the highest number of carriers is produced in HNCs with the largest volume (the production rate of electrons and holes behaves as $g_i \propto \sigma_{abs,i}$ where the average absorption cross-section of the HNCs $\sigma_{abs,i}$ is proportional to their volume in the Rayleigh regime). Nonetheless, apparently in conflict with this behavior, the final size of deposited Au NDs is the largest for short HNCs. This is likely due to the late-stage secondary nucleation, which systematically happens on the $CuInS_2$ part of long HNCs (Figure 3).

3.3. Late-Stage Growth of Gold ND on $CuInS_2$ and Au_2S Formation on $Cu_{2-x}S$ in Long HNCs

Once the growth of the Au ND on the $Cu_{2-x}S$ part is close to completion (around $t \approx 2(\tau_e)_{Cu_{2-x}S}$ according to Equations 5 and 6, modeling (Section S15, Supporting Information), and data fitting of the Au ND growth law presented in Figure 5c), further gold ion reduction should occur on the $CuInS_2$ surface to grow a new gold ND while concomitantly part of the holes can oxidize Au° from the already existing ND deposited on the $Cu_{2-x}S$ part to trigger the formation of Au_2S on the Au/$Cu_{2-x}S$ part. This mechanism, in agreement with TEM observations, is described by (Equation 7):

$$
\begin{cases}
\dfrac{d[e]}{dt} = \left(g - k_r\,[e]\,[h]\right)_{\text{bulk NC}} - \left(k_e^{CuInS_2}\,[e]\,\left[Au^{3+}\right]_{CuInS_2}\right)_{\text{ads } CuInS_2} \\
\dfrac{d[h]}{dt} = \left(g - k_r\,[e]\,[h]\right)_{\text{bulk NC}} - \left(k_h^{Au^+}\,[h]\,\left[Au^0\right]_{Cu_{2-x}S}\right)_{\text{bulk Au/Cu}_{2-x}\text{S}} - \left(k_h^{HS}\,[h]\,[HS]\right)_{\text{ads NC}} \\
\dfrac{d\left[Au^0\right]_{CuInS_2}}{dt} = -\dfrac{d\left[Au^{3+}\right]_{CuInS_2}}{dt} = \left(k_e^{CuInS_2}\,[e]\,\left[Au^{3+}\right]_{CuInS_2}\right)_{\text{ads } CuInS_2} \\
\dfrac{d\left[Au^0\right]_{Cu_{2-x}S}}{dt} = -\left(k_h^{Au^+}\,[h]\,\left[Au^0\right]_{Cu_{2-x}S}\right)_{\text{bulk Au/Cu}_{2-x}\text{S}} \\
\text{Pure vacancy filling}\begin{cases}
\dfrac{d\left[Au^+\right]_{Cu_{2-x}S}}{dt} = \left(k_h^{Au^+}\,[h]\,\left[Au^0\right]_{Cu_{2-x}S} - k_{Au_2S}\left[S^{2-}\right]\left[Au^+\right]_{Cu_{2-x}S}\right)_{\text{bulk Au/Cu}_{2-x}\text{S}} \\
\dfrac{d[Au_2S]}{dt} = -\dfrac{d\left[S^{2-}\right]}{dt} = \left(k_{Au_2S}\left[S^{2-}\right]\left[Au^+\right]_{Cu_{2-x}S}\right)_{\text{bulk Au/Cu}_{2-x}\text{S}}
\end{cases} \\
\text{Pure cation exchange}\begin{cases}
\dfrac{d\left[Au^+\right]_{Cu_{2-x}S}}{dt} = \left(k_h^{Au^+}\,[h]\,\left[Au^0\right]_{Cu_{2-x}S} - k_{AuCu}\left[Cu^+\right]\left[Au^+\right]_{Cu_{2-x}S}\right)_{\text{bulk Au/Cu}_{2-x}\text{S}} \\
\dfrac{d[Au_2S]}{dt} = -\dfrac{1}{2}\,\dfrac{d\left[Cu^+\right]}{dt} = \left(k_{AuCu}\left[Cu^+\right]\left[Au^+\right]_{Cu_{2-x}S}\right)_{\text{bulk Au/Cu}_{2-x}\text{S}}
\end{cases}
\end{cases}
\tag{7}
$$

Late-Stage Gold ND Growth Modeling on $CuInS_2$. The description of the second growth of Au NDs on the surface of long $CuInS_2$ parts is conceptually analogous to the previous one on $Cu_{2-x}S$ and detailed in Section S16 (Supporting Information), except that it is delayed by the completion time $\approx 2(\tau_e)_{Cu_{2-x}S}$ of the first growth of Au ND on $Cu_{2-x}S$; hole consumption also includes, in this case, the Au ND oxidation on the $Cu_{2-x}S$ part. The stationary concentration of electrons is, then, formally given by: $[e]_{sta} = \sqrt{\frac{(k_h^{Au^+}[Au^0]_{Cu_{2-x}S} + k_h^{HS}[HS]_{ads})\cdot g}{k_r \cdot k_e^{CuInS_2}[Au^{3+}]_{CuInS_2,ads}}}$.

Nonetheless, as hole scavenging is still dominated by the high concentration of methanol at the surface $[HS]_{ads}$, we expect $k_h^{Au^+}[Au^0]_{Cu_{2-x}S} \ll k_h^{HS}[HS]_{ads}$, so that: $[e]_{sta} \approx \sqrt{\frac{k_h^{HS}[HS]_{ads}\cdot g}{k_r \cdot k_e^{CuInS_2}[Au^{3+}]_{CuInS_2,ads}}}$. The new photo-reduction time scale of gold ions on $CuInS_2$ is $(\tau_e)_{CuInS_2} = \sqrt{\frac{k_r \beta_{CuInS_2}[Au^{3+}]_0}{k_e^{CuInS_2}\cdot k_h^{HS}[HS]_{ads}\cdot g C_{Au}}}$ and taking into account the delay of the second growth stage, $\Delta t = t - 2(\tau_e)_{Cu_{2-x}S} \geq 0$, we directly get (Equation 8):

$$
\left[Au^0\right]_{CuInS_2}\left(\Delta t \leq 2(\tau_e)_{CuInS_2}\right) = \beta_{CuInS_2}\left[Au^{3+}\right]_0 \cdot \frac{\Delta t}{(\tau_e)_{CuInS_2}} \cdot \left|1 - \frac{\Delta t}{4(\tau_e)_{CuInS_2}}\right| \tag{8}
$$

Leading to the growth law (Equation 9):

$$
Y\,[HNC]\,V\left(\Delta t \leq 2(\tau_e)_{CuInS_2}\right) = \nu_{Au}\,\beta_{CuInS_2}\left[Au^{3+}\right]_0 \frac{\Delta t}{(\tau_e)_{CuInS_2}} \cdot \left|1 - \frac{\Delta t}{4(\tau_e)_{CuInS_2}}\right| \tag{9}
$$

where $V = \pi D^3 \kappa(\bar{\theta})/8 \approx \pi D^3/6$ is the volume of the Au ND on $CuInS_2$ ($\bar{\theta} \approx 180°$). If we plot again $D[\frac{Y[HNC]}{[Au^{3+}]_0}]^{1/3}$ as a function of $\Delta t/(\tau_e)_{CuInS_2} \sim \sqrt{[HNC]\cdot I/[Au^{3+}]_0}\cdot \Delta t$, including the time delay of $2(\tau_e)_{Cu_{2-x}S}$ to the completion of the first Au ND growth onto $Cu_{2-x}S$, we obtain the rescaling illustrated in **Figure 6a**.

Late Stage Gold ND Growth on $CuInS_2$, Data Analysis. The full set of measurements performed under various conditions (variations in exposure time t, concentration $[Au^{3+}]_0$ and beam intensity I) effectively collapses onto the predicted single master behavior. Scaling onto a master behavior is, once again, observed over more than one order of magnitude in rescaled time, which is expected since the deposition mechanism is conceptually the same on both parts $Cu_{2-x}S$ and $CuInS_2$. Moreover, we can deduce the diameter at completion from the overall fit: $D_{\infty,CuInS_2} = 0.16[\frac{[Au^{3+}]_0}{Y\cdot[\text{Long HNC}]}]^{1/3}$ nm. Then, using $\bar{Y}_{CuInS_2} = 70\%$ and $\bar{\theta} \approx 180°$ on $CuInS_2$ ($\kappa(\bar{\theta}) \approx 4/3$), a value of $\beta_{CuInS_2} = (11.54 \pm 1.23)$ % is obtained. So, the amount of deposited gold on long HNCs (including the first deposition on $Cu_{2-x}S$ and the second on $CuInS_2$) represents a total of $\beta_{Cu2S} + \beta_{CuInS2} \approx (7.11 + 11.54)\% \approx 20\%$; this value is lower than that found previously for a mixture of $Cu_{2-x}S$ seeds and short HNCs, presumably because the electric field gradient generated is much smaller in the case of long HNCs than of short ones.

Late-Stage Modeling Au_2S Transformation of $Au/Cu_{2-x}S$. Concomitantly, experiments showed the formation of Au_2S in the $Au/Cu_{2-x}S$ part of the long HNCs (Figure 4), likely triggered by the photo-oxidation of the Au^0 initially photodeposited on the $Cu_{2-x}S$ part. We, thus, propose to calculate the dynamics of the photo-assisted production of Au_2S on $Cu_{2-x}S$ and see whether it is coherent with experimental observations. Two mechanisms are proposed in the literature with a possible simultaneity: elimination of copper vacancies in $Cu_{2-x}S$ with $x = 0.4$ and Cu^+/Au^+ cation exchange.[51] The main stages to determine $[Au_2S](\Delta t)$ from (Equation 7), based on these two mechanisms considered separately, are detailed in Section S17 (Supporting Information).

i) If we assume that the growth of the gold ND on the $Cu_{2-x}S$ part almost reached completion during the first stage, then the initial amount of Au^0 at $t \approx 2(\tau_e)_{Cu_{2-x}S}$ for the

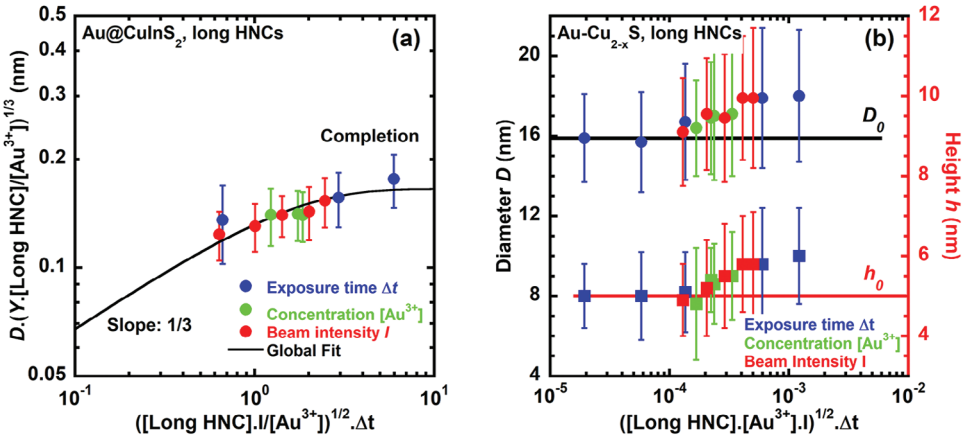

Figure 6. a) Plot of the rescaled single Au ND diameter $D \cdot (Y[\mathrm{HNC}]/[\mathrm{Au}^{3+}]_0)^{1/3}$ onto the $CuInS_2$ fragment of long HNCs, as a function of the reduction rescaled time $\Delta t/(\tau_e)_{CuInS_2} \propto \sqrt{[\mathrm{HNC}] \cdot I/[\mathrm{Au}^{3+}]_0} \cdot \Delta t$, when varying the exposure time Δt, the initial gold ion concentration $[\mathrm{Au}^{3+}]_0$, and the beam intensity I, all the other parameters being constant. The fitting curve is composed of two successive behaviors, the early one predicted by (Equation 9), followed by an exponential saturation in $\Delta t/(\tau_e)_{CuInS_2}$ up to the completion of the photoreaction in the finite volume of the solution (1 cm^3). b) Variations of the height h and the diameter D of the Au-$Cu_{2-x}S$ part as a function of the rescaled oxidation time $\Delta t/(\tau_h)_{Cu_{2-x}S} \propto \sqrt{[\mathrm{Au}^{3+}]_0 \cdot [\mathrm{HNC}] \cdot I} \cdot \Delta t$, when varying the exposure time Δt, the initial gold ion concentration $[\mathrm{Au}^{3+}]_0$, and the beam intensity I, all the other parameters being fixed.

second stage is $[\mathrm{Au}^0]_{Cu_{2-x}S}(t \approx 2(\tau_e)_{Cu_{2-x}S}) = \beta_{Cu_{2-x}S}[\mathrm{Au}^{3+}]_0$. Also, carrier stationarity is now given by: $k_e^{CuInS_2}[\mathrm{e}]\,[\mathrm{Au}^{3+}]_{CuInS_2,ads} = [\mathrm{h}]\,(k_h^{Au^+}[\mathrm{Au}^0]_{Cu_{2-x}S} + k_h^{HS}[\mathrm{HS}]_{ads})$. The stationary hole concentration in high field conditions becomes: $[\mathrm{h}]_{sta} = \sqrt{\frac{k_e^{CuInS_2}[\mathrm{Au}^{3+}]_{CuInS_2,ads} \cdot g}{k_r \cdot (k_h^{Au^+}[\mathrm{Au}^0]_{Cu_{2-x}S} + k_h^{HS}[\mathrm{HS}]_{ads})}}$, where $[\mathrm{Au}^{3+}]_{CuInS_2}(\Delta t \le 2(\tau_e)_{CuInS_2}) = \beta_{CuInS_2}[\mathrm{Au}^{3+}]_0\,(1 - \frac{\Delta t}{2(\tau_e)_{CuInS_2}})^2$ when methanol hole scavenging is dominating ($k_h^{Au^+}[\mathrm{Au}^0]_{Cu_{2-x}S} \ll k_h^{HS}[\mathrm{HS}]_{ads}$); see Section S17 (Supporting Information).

ii) The gold oxidation step is described by the decreasing variation of $[\mathrm{Au}^0]_{Cu_{2-x}S}$: $\frac{d[\mathrm{Au}^0]_{Cu_{2-x}S}}{dt} \approx -k_h^{Au^+}[\mathrm{h}]_{sta}[\mathrm{Au}^0]_{Cu_{2-x}S}$. Defining a new scavenging time scale: $(\tau_h)_{Cu_{2-x}S} = \frac{1}{k_h^{Au^+}}\sqrt{\frac{k_r \cdot k_h^{HS}[\mathrm{HS}]_{ads}}{k_e^{CuInS_2}\beta_{CuInS_2}[\mathrm{Au}^{3+}]_0 \cdot C_{CuInS_2} \cdot g}}$, we find (Equation 10):

$$[\mathrm{Au}^0]_{Cu_{2-x}S}\left(\Delta t \le 2(\tau_e)_{CuInS_2}\right) \approx \beta_{Cu_{2-x}S}[\mathrm{Au}^{3+}]_0 \cdot exp\left(-\frac{\Delta t}{(\tau_h)_{Cu_{2-x}S}}\right) \quad (10)$$

iii) Given $[\mathrm{Au}^0]_{Cu_{2-x}S}(\Delta t)$, the Au^+ production step is described either by $\frac{d[\mathrm{Au}^+]_{Cu_{2-x}S}}{dt} \approx k_h^{Au^+}[\mathrm{h}]_{sta}[\mathrm{Au}^0]_{Cu_{2-x}S} - k_{Au_2S}[\mathrm{S}^{2-}][\mathrm{Au}^+]_{Cu_{2-x}S}$ (elimination of copper vacancies), or $\frac{d[\mathrm{Au}^+]_{Cu_{2-x}S}}{dt} \approx k_h^{Au^+}[\mathrm{h}]_{sta}[\mathrm{Au}^0]_{Cu_{2-x}S} - k_{AuCu}[\mathrm{Cu}^+][\mathrm{Au}^+]_{Cu_{2-x}S}$ (cation exchange). If we assume $[\mathrm{h}]_{sta} \gg \{[\mathrm{S}^{2-}]_0, [\mathrm{Cu}^+]\}$, since the amount of available S^{2-} and Cu^+ is limited by the small finite size of the $Cu_{2-x}S$ portion and experiments are performed in "high field" conditions, we find (Equation 11):

$$[\mathrm{Au}^+]_{Cu_{2-x}S}(\Delta t) = \beta_{Cu_{2-x}S}[\mathrm{Au}^{3+}]_0 \cdot \left[1 - exp\left(-\frac{\Delta t}{(\tau_h)_{Cu_{2-x}S}}\right)\right] \quad (11)$$

when considering the initial condition $[\mathrm{Au}^+]_{Cu_{2-x}S}(\Delta t = 0) = 0$.

iv) The third step of the resolution consists of using the expression of $[\mathrm{Au}^+]_{Cu_{2-x}S}(\Delta t)$ for the elimination of copper vacancies: $\frac{d[\mathrm{S}^{2-}]}{dt} = -k_{Au_2S}[\mathrm{S}^{2-}][\mathrm{Au}^+]_{Cu_{2-x}S}$ or the cation exchange: $\frac{d[\mathrm{Cu}^+]}{dt} = -k_{AuCu}[\mathrm{Cu}^+][\mathrm{Au}^+]_{Cu_{2-x}S}$. On the one hand, the involved concentration $[\mathrm{S}^{2-}](\Delta t)$ corresponds to available ones from $Cu_{2-x}S$ vacancies ($x = 0.4$), and the involved concentration $[\mathrm{Cu}^+](\Delta t)$ to that associated to the $Cu_{2-x}S$ part. On the other hand, the amount of oxidized Au^+ is limited by the Au ND deposited on $Cu_{2-x}S$ at the completion of the early growth. Then, the initial availability is given by $Min\{[\mathrm{S}^{2-}](\Delta t = 0),\ \frac{1}{2} \cdot \beta_{Cu_{2-x}S}[\mathrm{Au}^{3+}]_0\}$ for the elimination of copper vacancies (the factor 1/2 comes from the stoichiometry) or, $Min\{[\mathrm{Cu}^+](\Delta t = 0),\ \beta_{Cu_{2-x}S}[\mathrm{Au}^{3+}]_0\}$ for the cation exchange. These amounts are estimated in Section S17 (Supporting Information) using the mean size of the gold ND deposited on $Cu_{2-x}S$ at completion (see Figure 5). They show that the limiting factor is $[\mathrm{S}^{2-}](\Delta t = 0)$ ($[\mathrm{S}^{2-}](\Delta t = 0) \approx 5.92\ 10^{-6}$ M $< \frac{1}{2}\beta_{Cu_{2-x}S}[\mathrm{Au}^{3+}]_0 = 7.25\ 10^{-6}$ M) for the elimination of copper vacancies, and the amount of deposited gold $\beta_{Cu_{2-x}S}[\mathrm{Au}^{3+}]_0$ for the cation exchange ($\beta_{Cu_{2-x}S}[\mathrm{Au}^{3+}]_0 = 1.45\ 10^{-5}$ M $< [\mathrm{Cu}^+](\Delta t = 0) = 4.73\ 10^{-5}$ M). After noting that $k_{Au_2S}\beta_{Cu_{2-x}S}[\mathrm{Au}^{3+}]_0 \cdot (\tau_h)_{Cu_{2-x}S} \sim \frac{[\mathrm{Au}_2\mathrm{S}]_{max}}{\{[\mathrm{S}^{2-}]_0, [\mathrm{Cu}^+]_0\}} \approx 1$ (see Section S17 (Supporting Information)), we deduce (Equation 12):

$$\{[\mathrm{S}^{2-}](\Delta t), [\mathrm{Cu}^+](\Delta t)\} = \{[\mathrm{S}^{2-}](\Delta t = 0), \beta_{Cu_{2-x}S}[\mathrm{Au}^{3+}]_0\} \times exp\left[1 - \left(\frac{\Delta t}{(\tau_h)_{Cu_{2-x}S}}\right) - exp\left(-\frac{\Delta t}{(\tau_h)_{Cu_{2-x}S}}\right)\right] \quad (12)$$

v) Then, the production of $[\mathrm{Au}_2\mathrm{S}](\Delta t)$ is obtained either from $\frac{d[\mathrm{Au}_2\mathrm{S}]}{dt} = -\frac{d[\mathrm{S}^{2-}]}{dt}$ (elimination of copper vacancies), or $\frac{d[\mathrm{Au}_2\mathrm{S}]}{dt} = -\frac{1}{2}\frac{d[\mathrm{Cu}^+]}{dt}$ (cation exchange). As $[\mathrm{Au}_2\mathrm{S}](\Delta t = 0) \approx 0$, the time variation of $[\mathrm{Au}_2\mathrm{S}](\Delta t)$ is eventually (Equation 13):

$$[Au_2S]\,(\Delta t) \approx \left\{ [S^{2-}]_0, \frac{\nu_{Au_2S}\beta_{Cu_{2-x}S}}{2} \right\} \cdot \left[1 - exp\left(1 - \left(\frac{\Delta t}{(\tau_h)_{Cu_{2-x}S}}\right) - exp\left(-\frac{\Delta t}{(\tau_h)_{Cu_{2-x}S}}\right)\right)\right] \quad (13)$$

$[Au_2S](\Delta t)$ is then expected to behave in a parabolic way at short times ($\frac{\Delta t}{(\tau_h)_{Cu_{2-x}S}} \ll 1$) and to saturate exponentially toward the maximum sulfide ion available $[S^{2-}](\Delta t = 0)$ (elimination of copper vacancies), or the total consumption of the gold ND $\beta_{Cu_{2-x}S}[Au^{3+}]_0/2$ (cation exchange), with the same kinetics driven by the scavenging time scale $(\tau_h)_{Cu_{2-x}S}$.

vi) Finally, as the transformation of $Cu_{2-x}S$ into Au_2S increases the unit volume of the crystal lattice by a factor ≈ 38%,[47] we expect that the dynamic production of Au_2S increases the volume $V(\Delta t)$ of the Au-$Cu_{2-x}S$ part as: $Y[HNC]\,[V(\Delta t) - V_0] = \nu_{Au_2S}\,[Au_2S](\Delta t)$, where V_0 is the initial volume of the $Cu_{2-x}S$ part in long HNCs, and $V(\Delta t)$ is the overall volume, measured from $D(\Delta t)$ and $h(\Delta t)$, minus $\pi D_0{}^2(h(\Delta t) - h_0)/4$, which represents the possible part of the $CuInS_2$ cylindrical core covered by the evolving Au-$Cu_{2-x}S$; this covering is illustrated by the increase of $h(\Delta t)$ during laser beam exposure while the overall length l of the long HNCs remains constant (Figure 3f; Figures S8 and S11, Supporting Information). Moreover, since the shape of the initial $Cu_{2-x}S$ part and its further transformation are very similar to spherical caps of respective heights h_0 and $h(\Delta t)$, and diameters D_0 and $D(\Delta t)$, we approximate volumes using the expression: $V(\Delta t) - V_0 = \frac{\pi}{6}\,h(\frac{3}{4}D^2 + h^2) - \frac{\pi D_0{}^2}{4}(h - h_0)$. We thus expect (Equation 14) for the two mechanisms considered separately:

$$V(\Delta t) \approx V_0 + \left\{ [S^{2-}]_0, \frac{\nu_{Au_2S}\beta_{Cu_{2-x}S}}{2} \right\} \frac{[Au^{3+}]_0}{Y[HNC]} \cdot \left[1 - exp\left(1 - \left(\frac{\Delta t}{(\tau_h)_{Cu_{2-x}S}}\right) - exp\left(-\frac{\Delta t}{(\tau_h)_{Cu_{2-x}S}}\right)\right)\right] \quad (14)$$

with the oxidation rescaled time $\frac{\Delta t}{(\tau_h)_{Cu_{2-x}S}} \propto \sqrt{[Au^{3+}]_0 \cdot [HNC] \cdot I} \cdot \Delta t$. Note that we cannot raise independent predictions for the height $h(\Delta t)$ and diameter $D(\Delta t)$ as mass conservation just considers the volume $V(\Delta t)$. Nonetheless, as $h(\Delta t)$ and $D(\Delta t)$ formally vary independently, we should also expect a rescaling when plotted as a function of $\frac{\Delta t}{(\tau_h)_{Cu_{2-x}S}}$. This expected data rescaling is illustrated in Figure 6b and convincingly shows that experiments performed in exposure time t, initial gold ion concentration $[Au^{3+}]_0$ and beam intensity I, all collapse onto single behaviors for both the diameter $D(\Delta t)$ and the height $h(\Delta t)$ over almost two orders of magnitude in rescaled time.

Late Stage Au_2S Transformation of Au/$Cu_{2-x}S$, Data Analysis. **Figure 7** eventually shows the predicted rescaling for the volume $V(\Delta t)$. The collapse of the volume data onto a single behavior is highly consistent, particularly when keeping in mind that plotting volumes instead of lengths drastically increases data dispersion.

Moreover, using the mean initial volume $V_0 = 549\ nm^3$ of the $Cu_{2-x}S$ part, the fit according to the model convincingly describes the overall dynamics up to exponential saturation ($V_\infty - V_0 = 76\ nm^3$), over almost two orders of magnitude in rescaled time (the correlation is 0.7). The predictions at completion from (Equation 14) for a "complete filling" of copper vacancies or a "complete exchange" of Au^+ can be estimated using i) the molecular volume $\nu_{Au_2S} = M_{Au_2S}/(N_A\rho_{Au_2S})$ of Au_2S, with the molar mass $M_{Au_2S} = 426.0$ g and the density $\rho_{Au_2S} = 11.0\ g\,cm^{-3}$, ii) $[HNC] = 2.54\ 10^{-9}$ M used in experiments, and iii) $\bar{Y}_{Cu_{2-x}S} = 70\%$. On the one hand, the filling of all copper vacancies involves $[S^{2-}](\Delta t = 0) \approx 5.92\ 10^{-6}$ M (see Section S17 (Supporting Information)), and the predicted maximum volume variation after filling all vacancies is $V_\infty - V_0 = \frac{\nu_{Au_2S}[S^{2-}](\Delta t=0)}{\bar{Y}[HNC]} \approx 210\ nm^3$. On the other hand, a complete cation exchange of all the Au^+ involves $\beta_{Cu_{2-x}S} = 7.11\%$ (for long HNCs) and $[Au^{3+}]_0 = 0.204$ mM (mostly used); the predicted maximum volume variation at completion is $V_\infty - V_0 = \frac{\nu_{Au_2S}\beta_{Cu_{2-x}S}[Au^{3+}]_0}{2\bar{Y}[HNC]} \approx 260\ nm^3$. In our experimental conditions, the two mechanisms lead to almost the same predicted volume change, thus preventing any insight into a possible prevailing mechanism. Experimentally, the volume change is given by the fit in Figure 7: $V_\infty/V_0 = 1 + 76/549$. The volume increase is thus 14%, smaller than the 38% expected for a complete conversion.[47] This difference may have several origins. One is based on unavoidable approximations to get analytic predictions. Another one concerns the fact that holes/electrons mobility-induced delays and trapping in crystal lattices are not considered in the rate equations. It shows nonetheless that the overall two-step prediction, from gold ND photodeposition to its transformation into Au_2S, remains quantitatively in the right order of magnitude. It results that 37% of the $Cu_{2-x}S$ allowed the formation of Au_2S at completion.

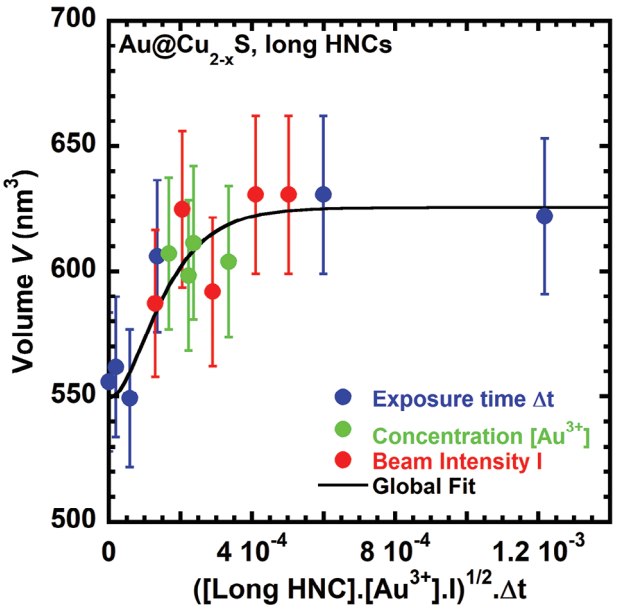

Figure 7. Volume change, $V(\Delta t)$, of the Au-$Cu_{2-x}S$ part of long HNCs by the photo-assisted production of Au_2S as a function of the same oxidation-rescaled time $\Delta t/(\tau_h)_{Cu2-xS}$ when varying exposure time Δt, the initial gold ion concentration $[Au^{3+}]_0$ and beam intensity I. The fit is performed using (Equation 14). The error in measured sizes corresponds to the standard deviation obtained on at least 200 measurements per data.

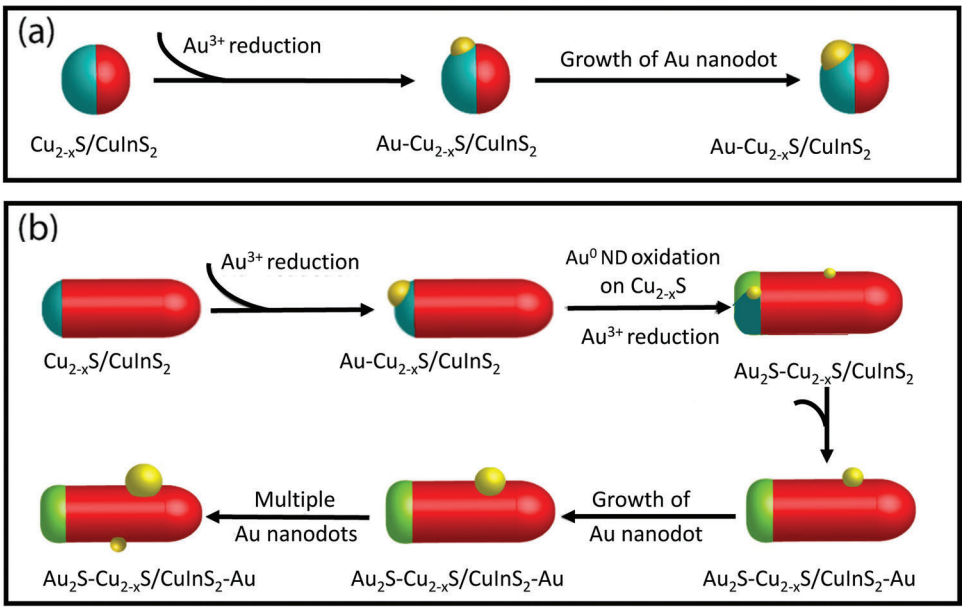

Figure 8. a,b) Schematic illustration of the proposed mechanisms of the Au ND laser-deposition on short a) and long b) Janus-type $Cu_{2-x}S/CuInS_2$ HNCs. The cyan part represents $Cu_{2-x}S$ and the red part, the elongated $CuInS_2$. The Au NDs are represented in yellow, and the green spherical caps indicate the transformation of the $Cu_{2-x}S$ tips by gold oxidation.

In conclusion, the predicted scaling for the second growth stage on long HNCs is well-established for the gold ND growth on the $CuInS_2$ part, and modeling of the photo-assisted production of Au_2S onto the initial $Cu_{2-x}S$ part seems highly coherent with the observations. Thus, the mechanisms involved during the entire dynamics of photodeposition, from the first stage of gold ND growth onto $Cu_{2-x}S$ to its second partial transformation into Au_2S concomitantly to the growth of a second gold ND at the surface of $CuInS_2$, are likely clarified by quantitative comparisons and may suggest a predictive approach to form nano-hetero-trimers from hetero-nanocrystals.

4. Discussion

As shown above, the outcome of Au photodeposition on the Janus-type $Cu_{2-x}S/CuInS_2$ HNCs strongly depends on the length of the $CuInS_2$ segment. For short HNCs, the Au NDs are exclusively deposited on the $Cu_{2-x}S$ segment near the hetero-interface, as depicted in **Figure** 8a. The size of the Au ND increases gradually with irradiation time, gold ion concentration, and/or photon flux, eventually reaching a stable size that remains unchanged even with prolonged exposure. The introduction of a $CuInS_2$ segment on the $Cu_{2-x}S$ NCs accelerates the gold ND growth rate and results in a larger final size as compared to Au ND grown on single-component $Cu_{2-x}S$ NCs. In sharp contrast, (Figure 8b), the gold photodeposition on long HNCs exhibits another sequential step. Fast deposition of a single Au ND on the $Cu_{2-x}S$ tip still occurs first as for short HNCs, but it is followed by a second stage characterized by the dynamic transformation of the Au-$Cu_{2-x}S$ part into another one, which presents both Au_2S and $Cu_{2-x}S$ domains (Figure 4). This process is concomitant with the deposition of Au NDs on the side of the elongated $CuInS_2$ segments.

In the initial step, gold ions are, in all cases, reduced to Au^0 and preferentially deposited on the $Cu_{2-x}S$ tips. This regiospecific reduction is probably due to i) the synergy between the small lattice mismatch between Cu_2S and Au that results in favorable epitaxial growth of Au NDs on the Cu_2S surface (the (102) planes of the hexagonal Cu_2S and the (111) planes of cubic Au have the same lattice distance of 2.4 Å),[55] ii) the high number of defects on the sides of $Cu_{2-x}S$ due to the high mobility of Cu^+ in the crystal lattice,[35] and iii) the slightly negative charge of $Cu_{2-x}S$ due to the low Cu^+ deficit. Under prolonged irradiation, we observed no modification of the Au NDs on short HNCs while, on long ones, Au NDs were oxidized to Au^+ and formed Au_2S domains in the $Cu_{2-x}S$ portion (compare Figure 3b,c), and another Au ND growth was triggered on the side of the $CuInS_2$ segment by the reduction of the Au^{3+} in solution.

The presence of a first single Au ND on the $Cu_{2-x}S$ segment intrinsically promotes charge separation, generating an electric field gradient within the HNCs[53] and strengthening the attraction of electrons to the Au-$Cu_{2-x}S$ part; the smaller the HNC, the higher the field gradient and charge separation, and the more intense the photon flux, the higher the amplitude of this electric field gradient. The resulting charge separation in short HNCs, for which the effect is the largest, thus prevents positive charges (holes) from reaching the Au-$Cu_{2-x}S$ domains and photo-oxidizing the Au ND. At the same time, it generates a sufficiently high electron deficit in the $CuInS_2$ part to prevent the growth of Au NDs by the photoreduction of Au^{3+}. Consequently, Au ND growth occurs strictly on $Cu_{2-x}S$, and the absence of positive charges makes this deposit very stable, while the absence of negative charges in $CuInS_2$ prevents the nucleation and growth of secondary Au NDs. Even if the carrier production increases with the volume of the HNCs, the resulting field gradient decreases with their length so that charge separation eventually becomes

less pronounced. Photogenerated electrons thus persist beyond a certain distance on the long $CuInS_2$ segments, facilitating the nucleation and growth of a second gold nanodot (ND) at a later stage. This growth occurs through the photoreduction of gold ions adsorbed on the $CuInS_2$ surface. Concomitantly, part of the hole consumption, mainly driven by methanol scavenging, can switch to the oxidation of the gold ND first deposited on $Cu_{2-x}S$ and favor the transformation into Au_2S in the Au-$Cu_{2-x}S$ domains. The inset of Figure 3e illustrates this decrease in the electric field gradient effect in the case of long HNCs. The mean distance between the hetero-interface $Cu_{2-x}S/CuInS_2$ and the Au ND grown on the $CuInS_2$ part follows a Gaussian distribution centered at 52 ± 13 nm. The deposition sites probably depend on the interplay between the gold reduction rate and the charge separation efficiency in HNCs. Finally, since we observe no second-stage photodeposition on short HNCs, we, therefore, assume that the charge separation efficiency in $Cu_{2-x}S/CuInS_2$ HNCs, is governed by the size of the elongated $CuInS_2$, as already discussed for CdSe/CdS dot-in-rod HNCs.[56,57] Consequently, the amplitude of the induced electric field gradient and the resulting efficiency in charge separation within the HNCs represent the cornerstone of understanding the different photo-induced processes involved in photodeposition and photoreactions. Laser exposure gives access to high electric field gradients, and the shorter the HNCs, the easier the formation of true Au-ND-based heteronanotrimers Au-$Cu_{2-x}S/CuInS_2$.

These gradients decrease along the length of the HNCs. However, they remain sufficiently high, unlike those induced by conventional lamps and LEDs, and provide the opportunity to initiate secondary redox processes leading to a different type of Au-ND-based heteronanotrimers (Au_2S-$Cu_{2-x}S$)/$CuInS_2$-Au. Such an approach is essential to shape heterogeneous semiconductor-metal nano-objects with light.

5. Conclusions

We have developed a laser-based photodeposition approach to grow Au nanodots onto binary-ternary Janus-type $Cu_{2-x}S/CuInS_2$ HNCs. The geometric distribution (e.g., number and location) and size of Au NDs can be well controlled by tuning the photon irradiance, exposure time, and concentration of the hole scavengers and Au precursors. The Au photodeposition rates on $Cu_{2-x}S/CuInS_2$ HNCs are higher than on $Cu_{2-x}S$ NCs, demonstrating that charge-carrier separation after photoexcitation is more efficient in the HNCs. Au NDs grow selectively on the $Cu_{2-x}S$ part of HNCs with both short and long $CuInS_2$ segments thanks to a better affinity. However, after the initial deposition of Au NDs on the $Cu_{2-x}S$ parts, long HNCs enter a second reaction stage, characterized by the transformation of part of the Au-$Cu_{2-x}S$ domain into Au_2S, with the concomitant deposition of Au NDs on the $CuInS_2$ segments.

The different results on the Au photodeposition on $Cu_{2-x}S$ seeds, short and long Janus-type $Cu_{2-x}S/CuInS_2$ are rationalized by a quantitative comparison with a model that describes the growth kinetics of the NDs, and their possible transformation, triggered by the photoproduction of electron-hole pairs within the NC seeds and the HNCs. Our results demonstrate that the key parameter controlling the architecture of Au-$Cu_{2-x}S/CuInS_2$ Janus-type heteronanotrimers is the amplitude of the photoinduced electric field gradient in the HNC, which is tailored by the size and shape of each fragment of the HNC. Moreover, kinetics modeling offers the possibility of gathering large sets of experiments, performed in various conditions, onto single master behaviors, which not only gives a quantitative description of photodeposition experiments but also allows for their rationalization when changing the size, the morphology, and the type of NCs. Our work thus provides novel experimental realization and theoretical insights into the design principles of multicomponent HNCs with controllable directional charge-carrier separation and paves the way for a predictability approach to make this design reliable and versatile.

6. Experimental Section

Materials: Indium nitrate hydrate ($In(NO_3)_3{\cdot}xH_2O$, 99.9%), copper acetylacetonate ($Cu(acac)_2$, 97%), copper(I) acetate (CuOAc, 97%), 1-dodecanethiol (DDT, ≥98%), oleic acid (OA, 90%), oleylamine (OLAM, 70%), potassium gold chloride ($KAuCl_4$, 99.995%), dodecylamine (DDA, 98%), anhydrous toluene, methanol, butanol, chloroform, and ethanol were purchased from Sigma–Aldrich, and used as received.

Synthesis of $Cu_{2-x}S/CuInS_2$ HNCs: The $Cu_{2-x}S/CuInS_2$ HNCs were synthesized by a two-stage seeded injection method according to a previously reported procedure.[39] $Cu_{2-x}S$ seed NCs were prepared by heating a mixture of $Cu(acac)_2$ (0.79 g, 3 mmol), 15 mL of OLAM, and 15 mL of DDT at 200 °C under N_2 protection for 2 h, followed by naturally cooling down to room temperature. The product was purified by the addition of an excess of isometric methanol and butanol solution and centrifuged at 2750 rpm for 10 min. The purification procedure was repeated 3 times. The $Cu_{2-x}S$ NCs were then redispersed in 12 mL of anhydrous toluene and stored in a glovebox for further use.

For a typical seeded injection reaction, 1 mL of the as-prepared $Cu_{2-x}S$ NCs seeds stock solution was precipitated using the washing step mentioned above. The black precipitate was redispersed in 5 mL of DDT. In the meantime, a mixture of $In(NO_3)_3{\cdot}xH_2O$ (0.06 g, 0.2 mmol) and 4 mL of OA was degassed for 30 min at 120 °C before heating to 240 °C under N_2 protection. At this temperature, the as-prepared $Cu_{2-x}S$ NCs solution was rapidly injected into the hot $In(NO_3)_3$–OA solution and the mixture was allowed to react for 40 min. The reaction solution was then naturally cooled down and washed with an excess of ethanol, followed by centrifugation at 2750 rpm for 10 min. The washing steps were repeated 3 times. The HNCs were finally redispersed in 5 mL of toluene and stored in a glovebox for further use.

Phase Transfer of $KAuCl_4$ from Water to Toluene: The phase transfer of $KAuCl_4$ from water to toluene was performed according to a previously reported approach.[58,59] To start, an 8 mM $KAuCl_4$ aqueous solution was prepared by dissolving $KAuCl_4$ (30.2 mg, 0.08 mmol) in 10 mL of deionized water. Then, 2 mL of this as-prepared $KAuCl_4$ solution was mixed with 2 mL of ethanol containing DDA (28 mg mL^{-1}). The mixture was vigorously shaken until a homogeneous solution was obtained, and the solution was then let stand for 1 h. Subsequently, 2 mL of anhydrous toluene was added to the mixture to allow the phase transfer from water to toluene. After 30 min, the upper layer, viz., toluene, turned from transparent to light yellow, indicating the successful phase transfer. The Au precursor in toluene was carefully extracted using a pipette and bubbled with argon for 10 min. Given the 100% efficiency of the phase transfer, the obtained 8 mM $KAuCl_4$ toluene solution was diluted to 4 mM for further experiments.

Laser-Induced Deposition of Au Nanodots onto $Cu_{2-x}S/CuInS_2$ HNCs: The $Cu_{2-x}S/CuInS_2$ HNCs solution was diluted ten in toluene under argon protection. Typically, 100 μL of the diluted HNCs solution, was mixed with 749 μL of anhydrous toluene, 51 μL of the 4 mM $KAuCl_4$-toluene solution, and 100 μL of methanol in the dark. The mixture was transferred to a 1 cm path-length sealed quartz cuvette and stirred at

300 rpm until the end of the experiments. The size of the laser in front of the cuvette was adjusted to be circular and 1 cm in diameter to be sure that the whole solution was completely exposed to the laser light. The excitation power and exposure time were finely tuned according to the experimental needs. Once the experiment was done, the reaction was quenched by turning off the laser and adding 1 mL of acetone. The product was collected by centrifugation at 4000 rpm for 10 min and washed once with 1 mL of isometric methanol/butanol followed by centrifugation at 4000 rpm for 10 min. The precipitate was redispersed in 0.5 mL of chloroform. All the experiments were performed at room temperature.

Characterization: Samples for transmission electron microscopy (TEM) analysis were prepared by drop-casting a solution of the NCs onto carbon-coated 200 mesh copper/nickel TEM grids. A few drops of chloroform were loaded on the same side of the grid to wash away some remaining metal salts. TEM analysis was performed with three microscopes, a JEOL JEM1400 Plus microscope operating at 120 kV, an FEI-Technai 12 microscope operating at 100 kV, and an FEI Technai 20 microscope operating at 200 kV. High-resolution TEM (HRTEM), high-angle annular dark-field scanning TEM (HAADF-STEM), and elemental mapping were performed on a Talos F200X (Thermo Fisher Scientific) or JEOL 2200 operated at 200 kV. The elemental maps were collected on an area of 1024 × 1024 pixels with an acquisition time of 5–10 min using Esprit software from Bruker. The elemental quantification was done by adding up all the counts in the entire spectrum for each channel and all pixels within the area of interest. Statistical analyses were performed on at least 100 gold nanodots. Each experiment was reproduced at least three times. Samples for X-ray diffraction (XRD) analysis were prepared by uniformly spreading dried NCs powder (~0.1 g) on a silicon wafer. XRD analyses were performed with a Bruker D2 Phaser, equipped with a Co Kα x-ray source with a wavelength of 1.79026 Å.

Supporting Information

Supporting Information is available from the Wiley Online Library or from the author.

Acknowledgements

C.X. and J. H. contributed equally to this work. This project has received financial support from the CNRS through the MITI interdisciplinary programs (Action MITI: Nouveaux Matériaux 2020 and 2021). F. Z. acknowledges the China Scholarship Council (CSC) for the financial support (grant number 201808440510). The TEM observations were performed on the microscopes of the Plateforme Aquitaine de Caractérisation des Matériaux (PLACAMAT, UAR 3626, CNRS, Univ. de Bordeaux, Pessac, France). The authors acknowledge Marion Gayot for her discussions and help. The HRTEM and STEM were obtained using equipment either at PLACAMAT or at Southern University of Science and Technology Core Research Facilities, and the authors acknowledge the technical support from Dongsheng He and Yang Qiu in SUSTech CRF.

Conflict of Interest

The authors declare no conflict of interest.

Data Availability Statement

The data that support the findings of this study are available in the supplementary material of this article.

Keywords

charge carriers, copper sulfide/copper indium sulfide, gold, heteronanotrimers, Janus structures, laser photodeposition

Received: August 29, 2024
Revised: August 30, 2024
Published online:

[1] Y. Liu, H. Ma, X. X. Han, B. Zhao, *Mater. Horiz.* **2021**, *8*, 370.
[2] J.-X. Fan, M.-D. Liu, C.-X. Li, S. Hong, D.-W. Zheng, X.-H. Liu, S. Chen, H. Cheng, X.-Z. Zhang, *Nanoscale Horiz.* **2017**, *2*, 349.
[3] C. Mao, Y. Xiang, X. Liu, Z. Cui, X. Yang, K. W. K. Yeung, H. Pan, X. Wang, P. K. Chu, S. Wu, *ACS Nano* **2017**, *11*, 9010.
[4] S. K. Dutta, S. K. Mehetor, N. Pradhan, *J. Phys. Chem. Lett.* **2015**, *6*, 936.
[5] J. K. Stolarczyk, S. Bhattacharyya, L. Polavarapu, J. Feldmann, *ACS Catal.* **2018**, *8*, 3602.
[6] M. Volokh, T. Mokari, *Nanoscale Adv* **2020**, *2*, 930.
[7] A. Kumar, P. Choudhary, A. Kumar, P. H. C. Camargo, V. Krishnan, *Small* **2021**, *18*, 2101638.
[8] Y. Ben-Shahar, D. Stone, U. Banin, *Chem. Rev.* **2023**, *123*, 3790.
[9] A. Zada, P. Muhammad, W. Ahmad, Z. Hussain, S. Ali, M. Khan, Q. Khan, M. Maqbool, *Adv. Funct. Mater.* **2020**, *30*, 1906744.
[10] K. Wenderich, G. Mul, *Chem. Rev.* **2016**, *116*, 14587.
[11] Y.-J. Yuan, D. Chen, Z.-T. Yu, Z.-G. Zou, *J. Mater. Chem. A* **2018**, *6*, 11606.
[12] K. Yang, Z. Yang, C. Zhang, Y. Gu, J. Wei, Z. Li, C. Ma, X. Yang, K. Song, Y. Li, Q. Fang, J. Zhou, *Chem. Eng. J.* **2021**, *418*, 129344.
[13] Z. Xi, H. Wan, Y. Ma, Y. Wu, L. Chen, H. Li, H. Zhou, J. Chen, G. Hou, *Prog. Org. Coat.* **2021**, *154*, 106197.
[14] G. Tian, C. Huang, X. Luo, Z. Zhao, Y. Peng, Y. Gao, N. Tang, S. Dsoke, *Chemistry* **2021**, *27*, 13774.
[15] Y. Zhou, Q. Li, Q. Han, L. Zhao, Y. Liu, Y. Wang, Z. Li, C. Dong, X. Sun, J. Yang, X. Zhang, F. Jiang, *Small* **2023**, *19*, 2303742.
[16] J.-H. Park, P. Ramasamy, S. Kim, Y. K. Kim, V. Ahilan, S. Shanmugam, J.-S. Lee, *Chem. Commun.* **2017**, *53*, 3277.
[17] W. van der Stam, A. C. Berends, C. de Mello Donega, *Chemphyschem* **2016**, *17*, 559.
[18] N. E. Motl, J. F. Bondi, R. E. Schaak, *Chem. Mater.* **2012**, *24*, 1552.
[19] A. Wolf, D. Hinrichs, J. Sann, J. F. Miethe, N. C. Bigall, D. Dorfs, *J. Phys. Chem. C* **2016**, *120*, 21925.
[20] J. L. Fenton, J. M. Hodges, R. E. Schaak, *Chem. Mater.* **2017**, *29*, 6168.
[21] X. Y. Gan, R. Sen, J. E. Millstone, *J. Am. Chem. Soc.* **2021**, *143*, 8137.
[22] H. Zhu, Y. Wang, C. Chen, M. Ma, J. Zeng, S. Li, Y. Xia, M. Gao, *ACS Nano* **2017**, *11*, 8273.
[23] Y. Zou, C. Sun, W. Gong, X. Yang, X. Huang, T. Yang, W. Lu, J. Jiang, *ACS Nano* **2017**, *11*, 3776.
[24] S. Sen, S. Shyamal, S. K. Mehetor, P. Sahu, N. Pradhan, *J. Phys. Chem. Lett.* **2021**, *12*, 11585.
[25] B. K. Patra, S. Khilari, D. Pradhan, N. Pradhan, *Chem. Mater.* **2016**, *28*, 4358.
[26] A. B. Ghosh, N. Saha, A. Sarkar, A. K. Dutta, S. K. Maji, B. Adhikary, *New J. Chem.* **2017**, *41*, 692.
[27] S.-Y. Tang, H. Medina, Y.-T. Yen, C.-W. Chen, T.-Y. Yang, K.-H. Wei, Y.-L. Chueh, *Small* **2019**, *15*, 1803529.
[28] A. B. Ghosh, N. Saha, A. Sarkar, A. K. Dutta, J. Satra, B. Adhikary, *Dalton Trans.* **2018**, *47*, 1071.
[29] H. Wen, H. Li, S. He, F. Chen, E. Ding, S. Liu, B. Wang, Y. Peng, *Nanoscale* **2018**, *10*, 2380.
[30] P. S. Dilsaver, M. D. Reichert, B. L. Hallmark, M. J. Thompson, J. Vela, *J. Phys. Chem. C* **2014**, *118*, 21226.
[31] M. D. Regulacio, M.-Y. Han, *Acc. Chem. Res.* **2016**, *49*, 511.
[32] X. Yu, R. Du, B. Li, L. Liu, Y. Zhang, *J. Phys. Chem. C* **2017**, *121*, 6712.
[33] A. Ganai, P. S. Maiti, L. Houben, R. Bar-Ziv, M. Bar Sadan, *J. Phys. Chem. C* **2017**, *121*, 7062.
[34] P. Kalisman, Y. Nakibli, L. Amirav, *Nano Lett.* **2016**, *16*, 1776.

[35] L.-W. Wang, *Phys. Rev. Lett.* **2012**, *108*, 085703.
[36] C. Coughlan, M. Ibáñez, O. Dobrozhan, A. Singh, A. Cabot, K. M. Ryan, *Chem. Rev.* **2017**, *117*, 5865.
[37] B. C. Steimle, J. L. Fenton, R. E. Schaak, *Science* **2020**, *367*, 418.
[38] Y. Zhai, J. C. Flanagan, M. Shim, *Chem. Mater.* **2017**, *29*, 6161.
[39] C. Xia, C. H. M. van Oversteeg, V. C. L. Bogaards, T. H. M. Spanjersberg, N. L. Visser, A. C. Berends, J. D. Meeldijk, P. E. de Jongh, C. de Mello Donega, *ACS Nano* **2021**, *15*, 9987.
[40] Q. Bai, I. Shupyk, L. Vauriot, J. Majimel, C. Labrugere, M.-H. Delville, J.-P. Delville, *ACS Nano* **2021**, *15*, 2947.
[41] G. Menagen, J. E. Macdonald, Y. Shemesh, I. Popov, U. Banin, *J. Am. Chem. Soc.* **2009**, *131*, 17406.
[42] G. Dukovic, M. G. Merkle, J. H. Nelson, S. M. Hughes, A. P. Alivisatos, *Adv. Mater.* **2008**, *20*, 4306.
[43] C. Xia, W. Wu, T. Yu, X. Xie, C. van Oversteeg, H. C. Gerritsen, C. de Mello Donega, *ACS Nano* **2018**, *12*, 8350.
[44] K. Wu, W. E. Rodríguez-Córdoba, Y. Yang, T. Lian, *Nano Lett.* **2013**, *13*, 5255.
[45] I. Essafri, A. Ghoufi, *Phys Rev E* **2019**, *99*, 062607.
[46] J. Hao, H. Liu, K. Wang, X. W. Sun, J.-P. Delville, M.-H. Delville, *ACS Nano* **2021**, *15*, 15328.
[47] E. A. Hernández-Pagán, O'A. Hara, S. L. Arrowood, J. R. McBride, J. M. Rhodes, S. T. Pantelides, J. E. Macdonald, *Chem. Mater.* **2018**, *30*, 8843.
[48] X. Ding, Y. Zou, J. Jiang, *J. Mater. Chem.* **2012**, *22*, 23169.
[49] T. Mokari, C. G. Sztrum, A. Salant, E. Rabani, U. Banin, *Nat. Mater.* **2005**, *4*, 855.
[50] S. E. Habas, P. Yang, T. Mokari, *J. Am. Chem. Soc.* **2008**, *130*, 3294.
[51] X. Wang, X. Liu, D. Zhu, M. T. Swihart, *Nanoscale* **2014**, *6*, 8852.
[52] C. R. Henry, *Cryst. Res. Technol.: J. Experiment. Indust. Crystallogra.* **1998**, *33*, 1119.
[53] H. Gerischer, *J. Phys. Chem.* **1984**, *88*, 6096.
[54] A. Mills, C. O'Rourke, K. Moore, *J. Photochem. Photobiol. A Chem.* **2015**, *310*, 66.
[55] Y. Kim, K. Y. Park, D. M. Jang, Y. M. Song, H. S. Kim, Y. Myung, J. Park, *J. Phys. Chem. C* **2010**, *114*, 22141.
[56] L. Amirav, A. P. Alivisatos, *J. Am. Chem. Soc.* **2013**, *135*, 13049.
[57] L. Amirav, A. P. Alivisatos, *J. Phys. Chem. Lett.* **2010**, *1*, 1051.
[58] S. Chakrabortty, G. Xing, Y. Xu, S. W. Ngiam, N. Mishra, T. C. Sum, Y. Chan, *Small* **2011**, *7*, 2847.
[59] J. Yang, L. Levina, E. H. Sargent, S. O. Kelley, *J. Mater. Chem.* **2006**, *16*, 4025.